

Mass profiles and galaxy orbits in nearby galaxy clusters from the analysis of the projected phase-space

Radosław Wojtak and Ewa L. Łokas

Nicolaus Copernicus Astronomical Center, Bartycka 18, 00-716 Warsaw, Poland

29 November 2021

ABSTRACT

We analyze kinematic data of 41 nearby ($z < 0.1$) relaxed galaxy clusters in terms of the projected phase-space density using a phenomenological, fully anisotropic model of the distribution function. We apply the Markov Chain Monte Carlo approach to place constraints on total mass distribution approximated by the universal NFW profile and the profile of the anisotropy of galaxy orbits. We find the normalization of the mean mass-concentration relation is $c = 6.9_{-0.7}^{+0.6}$ at the virial mass $M_v = 5 \times 10^{14} M_\odot$. By comparison with the calibration from cosmological N -body simulations it is demonstrated that this result is fully consistent with σ_8 from WMAP1 data release and agrees at $\sim 1\sigma$ level with that from WMAP5. Assuming a one-to-one correspondence between σ_8 and the normalization of the mass-concentration relation in the framework of the concordance model we estimate the normalization of the linear power spectrum to be $\sigma_8 = 0.91_{-0.08}^{+0.07}$. Our constraints on the parameters of the mass profile are compared with estimates from X-ray observations and other methods based on galaxy kinematics. We also study correlations between the virial mass and different mass proxies including the velocity dispersion, the X-ray temperature and the X-ray luminosity. We demonstrate that the mass scaling relations with the velocity dispersion and the X-ray temperature are fully consistent with the predictions of the virial theorem.

We show that galaxy orbits are isotropic at the cluster centres (with the mean ratio of the radial-to-tangential velocity dispersions $\sigma_r/\sigma_\theta = 0.97 \pm 0.04$) and radially anisotropic at the virial sphere (with the mean ratio $\sigma_r/\sigma_\theta = 1.75_{-0.19}^{+0.23}$). Although the value of the central anisotropy appears to be universal, the anisotropy at the virial radius differs between clusters within the range $1 \lesssim (\sigma_r/\sigma_\theta) \lesssim 2$.

Utilizing the Bautz-Morgan morphological classification and information on the prominence of a cool core we select two subsamples of galaxy clusters corresponding to less and more advanced evolutionary states. It is demonstrated that less evolved clusters have shallower mass profiles and their galaxy orbits are more radially biased at the virial sphere. This property is consistent with the expected evolution of the mass profiles as well as with the observed orbital segregation of late and early type galaxies.

Key words: galaxies: clusters: general – galaxies: kinematics and dynamics – cosmology: dark matter

1 INTRODUCTION

Kinematic data for galaxy clusters offer a unique possibility to study their mass distribution and the orbits of the galaxies within them. Depending on the quality of data sample and the purpose of the analysis a number of methods of data modelling has been proposed, from the mass estimate based on the virial theorem (Heisler et al. 1985; Girardi et al. 1998), the Jeans analysis with the two

even velocity moments (Łokas & Mamon 2003) and the caustic technique (Diaferio & Geller 1997) to the recently presented kinematic deprojection with the mass inversion (Mamon & Boué 2010) and the projected phase-space analysis with a fully anisotropic model of the distribution function (Wojtak et al. 2009). There is no doubt that the component which is best constrained with all methods of data modelling is the mass profile. The analysis of galaxy kinematics

in nearby galaxy clusters revealed that the mass distribution is consistent with the universal NFW (Navarro et al. 1997) profile (see e.g. Biviano & Girardi 2003; Lokas et al. 2006; Rines & Diaferio 2006), which was confirmed in other studies based on X-ray observations (see e.g. Pointecouteau et al. 2005) or lensing data (e.g. Comerford et al. 2006). On the other hand, constraints on the parameters of the universal density profile of individual clusters from galaxy kinematics are available for a very limited number of objects (see Lokas et al. 2006; Wojtak & Lokas 2007). One of the main aims of this work is to provide robust estimates of these parameters for a statistically significant sample of nearby ($z < 0.1$) galaxy clusters.

Constraining the anisotropy of galaxy orbits from kinematic data is a difficult task. The main problem arises from the so-called mass-anisotropy degeneracy which occurs in the Jeans analysis of the velocity dispersion profile (Merritt 1987). In order to break this degeneracy a few solutions have been proposed. Binney & Mamon (1982) derived the velocity anisotropy profile by combining the Jeans standard analysis with an independent constraint on the mass profile. This approach was adopted by several authors who used the estimate of the mass profile from the kinematics of ellipticals whose orbits appear to be distributed isotropically (Biviano & Katgert 2004), lensing observations (Natarajan & Kneib 1996) or X-ray data (Benatov et al. 2006; Hwang & Lee 2008). Another method to solve the problem of the mass-anisotropy degeneracy relies on modelling the degree of non-gaussianity in the velocity distribution (Merrifield & Kent 1990). A way to account for this effect is to use two even velocity moments (Lokas & Mamon 2003; Lokas et al. 2006). Apart from this, in a few attempts a full model of the distribution function has been used, but in all cases a flat anisotropy profile was assumed (see e.g. van der Marel et al. 2000; Mahdavi & Geller 2004). Nevertheless, this method is still promising. As shown by Wojtak et al. (2009) in a series of tests on mock kinematic data, the projected phase-space analysis with a suitable model of the distribution function proposed by Wojtak et al. (2008) allows to place robust constraints on the spatial variation of the orbital anisotropy within the virial sphere as well as on the total mass profile. In this paper, we follow the method described in Wojtak et al. (2009) to constrain the orbital anisotropy at the cluster centres and around the virial radius.

Most measurements of the orbital anisotropy in galaxy clusters have been obtained under the assumption of a flat profile. All results are consistent within errors with isotropic orbits (see e.g. van der Marel et al. 2000; Rines et al. 2003; Mahdavi & Geller 2004; Lokas et al. 2006; Wojtak & Lokas 2007). Several studies were devoted to constraining the spatial variation of the orbital anisotropy. The analysis of galaxy kinematics of individual clusters points to rather isotropic orbits, although the anisotropy exhibits a significant scatter between clusters (see e.g. Natarajan & Kneib 1996; Benatov et al. 2006; Hwang & Lee 2008). More robust constraints on the anisotropy profile were obtained in the analysis of the composite clusters resulting from combining a number of kinematic data sets into one. It was demonstrated that the orbits of early type galaxies tend to be isotropic within the virial sphere, whereas late type galaxies are on predominantly radial orbits at the virial radius

(Adami et al. 1998; Biviano & Katgert 2004). This property is referred to as the orbital segregation and is commonly attributed to the orbital evolution from radially dominated orbits for spirals to isotropic ones for ellipticals. We note, however, that the orbital structure of both morphological types of galaxies can hardly be reconciled with the result of global isotropy. This problem is also addressed in this paper.

The paper is organized as follows. In section 2, we describe our cluster sample as well as kinematic data and the method of interloper removal. In section 3, we outline the details of our method of the projected phase-space analysis. The results of the analysis are presented in section 4. In the same section, we discuss the constraints on the mass-concentration relation and study the mass scaling relations. Section 5 is devoted to comparison between our constraints on the parameters of the mass profile and those found in the literature and based on other methods. In section 6, we present two tests of consistency between the data and some assumptions underlying our analysis. The summary follows in section 7. In this work, we adopted a flat Λ CDM cosmology with density parameter $\Omega_m = 0.3$ and the Hubble constant $H_0 = 70 \text{ km s}^{-1} \text{ Mpc}^{-1}$.

2 DATA

2.1 Cluster selection

The primary criterion for cluster selection is the number of galaxies with spectroscopic redshifts per cluster. An optimum choice of a threshold for this number should result from the consideration of two contradictory effects. On one hand, the quality of statistical reasoning requires the number of redshifts to be as large as possible, but on the other we wish to build a sample with a statistically significant number of clusters which means that we also have to include clusters with a rather low number of spectroscopic redshifts. Trying to find a compromise we checked the number of available redshifts per cluster, as provided by NASA/IPAC Extragalactic Database (NED). We found that the optimal choice for the purpose of our analysis is to consider clusters with at least 70 galaxies within the aperture of 2.5 Mpc and with velocities from the range $\pm 4000 \text{ km s}^{-1}$ in the rest frame of the cluster. The radius of the aperture equals to the virial radius of massive galaxy clusters and its role is to truncate all clusters to the approximate size of the virial sphere (in projection). The velocity range $\pm 4000 \text{ km s}^{-1}$ is a commonly used velocity cut-off which allows to perform a preliminary separation of cluster members from the interlopers (galaxies of background or foreground).

The second criterion for cluster selection concerns their dynamical state. The reason for considering this property is the fact that the basic assumption underlying our method of dynamical analysis is the state of equilibrium. It means that our sample should be possibly free of dynamically disturbed clusters, especially major mergers. In order to identify such clusters we studied X-ray images of clusters obtained with ASCA (Horner 2001), XMM-Newton (Snowden et al. 2008) and ROSAT (Schuecker et al. 2001) satellites. We rejected all clusters whose images exhibit signatures of merger activity in the form of clearly visible distortions (e.g. A3667) or the presence of massive subclusters (e.g. A3558, the most massive cluster in the Shapley Concentration).

Another approach to assess the dynamical state of clusters was to study the general properties of galaxy kinematics. This method was particularly important in the case of clusters for which X-ray data were not available. Following this approach, we excluded all clusters with clearly asymmetric or bimodal velocity distributions which are good signatures of a merger or at least an accidental alignment of some structures. Let us note that the analysis of galaxy kinematics was carried out after the proper removal of interlopers (see subsection 2.4).

As an independent test, we also checked for the presence of a cool core which appears to correlate with the dynamical state of clusters (Burns et al. 2008; Sanderson, Edge & Smith 2009; Hudson et al. 2010) and may be regarded as an indicator of how relaxed the cluster is. We note, however, that the presence of a cool core was a secondary criterion of our selection. We used this criterion only in cases when the conclusions drawn from the kinematics or the X-ray image seemed to be ambiguous or contradictory.

Finally, we also excluded clusters which appear to be accompanied by other clusters at comparable redshifts and relative positions on the sky smaller than 5 Mpc which is around twice the expected virial radius for a typical cluster. The majority of them are binary clusters at the initial state of merging, e.g. A399 and A401. The main reason for rejecting these systems is the fact that their velocity diagrams are severely contaminated by galaxies from neighbouring clusters. Due to the proximity of these clusters both on the sky and in redshift space, velocity diagrams overlap and the selection of cluster members becomes impossible or at least highly ambiguous.

2.2 Cluster sample

In order to find all nearby ($z < 0.1$) galaxy clusters which satisfy selection criteria described above we searched NED and the recently published, but not yet included in NED, spectroscopic data from WINGS (The WIdE field Nearby Galaxy cluster Survey) which is a photometric and spectroscopic survey of a few tens of nearby galaxy clusters (Cava et al. 2009). The final sample resulting from our data mining consists of 41 galaxy clusters, out of which 40 are rich clusters from the Abell catalogue (Abell 1958; Abell, Corwin & Olowin 1989) and one (MKW 4) is a poor cluster containing a cD galaxy (Morgan, Kayser & White 1975). Table 1 provides the list of all clusters as well as their basic observational properties, such as the heliocentric redshift z , the number of spectroscopic redshifts within the aperture of 2.5 Mpc and the velocity range $\pm 4000 \text{ km s}^{-1}$ around the mean N_{tot} and after the removal of interlopers (see subsection 2.4) N_{mem} .

All clusters in Table 1 are relaxed objects in terms of merger activity. However, we cannot expect that the whole cluster sample is completely uniform in terms of the evolutionary stage. In order to check this, we searched for two indirect indicators of cluster evolution. The first indicator is the presence of a cool core. As shown by Burns et al. (2008) and Hudson et al. (2010), the survival of a cool core in nearby galaxy clusters is likely associated with the quiescent phase of recent history, when the cluster has not experienced major mergers. Therefore the clusters which possess

Name	z	N_{tot}	N_{mem}	B-M type	CC
A0085	0.0551	325	317	I	yes ^a
A0119	0.0442	215	211	II-III	no ^a
A0133	0.0566	75	75	I-II	yes ^a
A0262	0.0163	141	135	III	yes ^a
A0376	0.0484	85	85	I-II	?
A0496	0.0329	324	313	I	yes ^a
A0539	0.0284	141	126	III	yes ^b
A0576	0.0389	241	214	III	yes ^a
A0671	0.0502	129	124	II-III	no ^d
A0779	0.0225	154	139	I-II	yes ^d
A0954	0.0932	68	66	I-II	?
A0957	0.0436	138	124	I-II	no ^d
A0978	0.0544	100	90	II	?
A1060	0.0126	369	365	III	yes ^a
A1139	0.0398	147	143	III	?
A1190	0.0751	137	122	II	?
A1314	0.0335	140	127	III	no ^d
A1650	0.0838	212	204	I-II	yes ^a
A1691	0.0721	118	110	II	?
A1767	0.0703	152	147	II	no ^d
A1773	0.0765	109	103	III	?
A1795	0.0625	177	163	I	yes ^a
A1809	0.0791	131	123	II	no ^d
A1983	0.0436	117	100	III	yes ^d
A2052	0.0355	150	107	I-II	yes ^a
A2063	0.0349	150	115	II	yes ^a
A2107	0.0411	88	85	I	yes ^c
A2142	0.0909	229	226	II	yes ^a
A2175	0.0951	93	87	II	?
A2415 ^w	0.0581	98	96	III	yes ^d
A2593	0.0413	230	210	II	no ^d
A2634	0.0314	223	185	II	yes ^a
A2670	0.0762	246	238	I-II	yes ^c
A2734	0.0625	174	149	III	no ^b
A3158	0.0597	148	145	I-II	no ^a
A3571	0.0391	180	168	I	yes ^a
A3581	0.0230	82	74	I	yes ^a
A3809 ^w	0.0623	105	99	III	?
A4059	0.0475	237	192	I	yes ^a
AS805	0.0139	159	148	I	?
MKW4	0.0200	132	124	I	yes ^a

Table 1. Observational properties of galaxy clusters selected for the analysis. The table includes the cluster name, heliocentric redshift (z), number of galaxy redshifts within the aperture 2.5 Mpc and the velocity range $\pm 4000 \text{ km s}^{-1}$ (N_{tot}), number of redshifts after interloper removal (N_{mem}), Bautz-Morgan morphological type (B-M type) and the comment on a cool core judged on the basis of: ^aHudson et al. (2010), ^bChen et al. (2007), ^cWhite (2000), ^dWhite, Jones & Forman (1997). Superscript w marks clusters from the WINGS survey.

cool cores are expected to be more relaxed. The second indicator is the morphological type. We used the Bautz-Morgan classification (Bautz & Morgan 1970) which describes the degree to which a cluster is dominated by the BCG (bright central galaxy). Like for many other morphological classifications of galaxy clusters, the Bautz-Morgan morphological type appears to correlate with the dynamical state of cluster evolution (Sarazin 1988). The early type clusters (I,I-II) which are more dominated by BCGs are more dynamically relaxed than clusters of late types (II-III,III).

The last two columns of Table 1 include information on the presence of a cool core and the Bautz-Morgan morpho-

logical type. Observational constraints on a cool core were obtained from the literature (White, Jones & Forman 1997; White 2000; Chen et al. 2007; Hudson et al. 2010). We note that the criteria used as the signatures of a cool core were not common to all authors and were mainly based on the inspection of such effects as a temperature drop at small radii, substantial mass deposition rate or sufficiently small cooling time in the cluster centres. Due to the fact that our cluster sample is optically selected, the X-ray data are not equally accessible for all objects. In particular, the information on the presence of a cool core was found for only 31 clusters (22 cool core clusters and 9 non-cool core clusters). For other clusters X-ray data are very limited and therefore insufficient to study this property.

The Bautz-Morgan morphological types of the clusters were obtained from NED. We note that this classification is not objective and may be treated as indicative only. Nevertheless, it allows us to divide our cluster sample into two classes, the early and late type clusters, which are thought to represent more and less advanced dynamical state of cluster evolution. A similar division of the clusters may be also carried out with respect to the presence of a cool core. In this approach cool core clusters are expected to be more dynamically evolved objects. A closer inspection of Table 1 shows that both classifications are clearly related to each other: the early type (I,I-II) clusters constitute 60 per cent of the cool core clusters and just 20 per cent of the non-cool core clusters. Let us note that this correlation, although not very tight, increases our confidence in using both classifications to assess the dynamical state of a cluster.

2.3 Velocity diagrams

The positions and redshifts of galaxies in the field of the clusters from Table 1 were obtained from NED. This database provides the most up-to-date compilation of many different kinds of extragalactic data, including spectroscopic redshifts. The majority of spectroscopic data stored in NED comes from data releases of large scale redshift surveys, e.g. the Sloan Digital Sky Survey (see Adelman-McCarthy et al. 2008, for the latest data release) or the 2dF Galaxy Redshift Survey (Colless et al. 2001), as well as a number of spectroscopic surveys dedicated to observations of individual galaxy clusters, e.g. the NOAO Fundamental Plane Survey (Smith et al. 2004). We note that the SDSS, the 2dF survey and the NFPS are the three dominant sources of redshift data for our cluster sample. For two clusters, A2415 and A3809, redshifts and positions come from the WINGS survey (Cava et al. 2009). We found that in both cases the number of redshifts provided by the catalogue of this survey is considerably higher than that provided by NED.

In order to calculate the projected clustercentric distances R of all galaxies one needs to find cluster centres. From the observational point of view, the cluster centre may be defined as the position of the X-ray emission peak or the location of the BCG. For clusters that are not dynamically disturbed both centres coincide with each other and both point very well to the minimum of the gravitational potential well. Since our cluster sample was constructed using optical data, we decided to assign cluster centres as the BCG positions. We found that 39 clusters from the sample have a well-confirmed central galaxy classified in NED as a cD

galaxy (27 clusters) or a BCG (12 clusters). For two clusters, A2415 and A3809, central bright galaxies were found by visual inspection of optical images. Both clusters have distinct, bright and extended ellipticals lying in the close vicinity of the cluster centre given by the catalogue of Abell clusters.

With cluster centres given by the positions of BCGs, we calculated the projected clustercentric distances of all galaxies. Except of a few clusters, the distances extend to $R_{\max} = 2.5$ Mpc which is a fixed size of the aperture in our analysis. Three exceptional clusters are A376, A2415 and A3809. The velocity diagram of the first of these is limited to the aperture of around 1.8 Mpc which may be the effect of the incompleteness of the spectroscopic survey or may reflect extreme compactness of this cluster. Galaxy distances of the other two clusters are limited by the aperture (around 1.5 Mpc) to which the WINGS survey is complete (see Cava et al. 2009). For the analysis of these three clusters we assumed $R_{\max} = 1.5$ Mpc. We note that an independent test for data completeness is presented in subsection 6.1.

2.4 Interloper removal

In order to separate cluster galaxies from the interlopers, i.e. galaxies of background or foreground, we applied the method proposed by den Hartog & Katgert (1996) which appears to be one of the most effective algorithms for interloper removal (see Wojtak et al. 2007; Wojtak & Lokas 2007). In this approach the interlopers are identified as galaxies with velocity along the line of sight exceeding a maximum velocity evaluated for a given projected radius R . Calculation of the maximum velocity $v_{\max}(R)$ is based on a toy model of cluster dynamics which assumes that galaxies follow circular orbits with velocity $v_{\text{cir}} = \sqrt{GM(r)/r}$ or fall towards the cluster centre with velocity $\sqrt{2}v_{\text{cir}}$. Evaluation of $v_{\max}(R)$ in such a model is simplified to finding the maximum of both velocity vectors projected onto the line of sight. We note that the interloper removal is an iterative procedure, i.e. the scheme is repeated several times until convergence is achieved. The mass $M(r)$ in each iteration is approximated by the virial mass estimator (Heisler et al. 1985) evaluated for all galaxies within the aperture $R = r$.

3 OVERVIEW OF THE METHOD

In this section, we summarize our method of statistical inference of the mass and anisotropy profiles from galaxy kinematics, as developed and described in detail in Wojtak et al. (2009). The method relies on the Markov Chain Monte Carlo (MCMC) analysis of galaxy distribution in the projected phase-space, i.e. the space of the projected radii R and velocities along the line of sight v_{los} , in terms of a properly parametrized model of the distribution function. The projected phase-space density $f_{\text{los}}(R, v_{\text{los}})$ is related to the distribution function $f(E, L)$ through the following integral

$$f_{\text{los}}(R, v_{\text{los}}) = 2\pi R \int_{-z_{\max}}^{z_{\max}} dz \iint_{E>0} dv_R dv_\phi f(E, L), \quad (1)$$

where z is the distance along the line sight from the cluster centre, v_R and v_ϕ are velocity components in cylindrical coordinates, E is the positively defined binding energy per unit

mass, L is the absolute value of the specific angular momentum and z_{\max} is the distance of equality between v_{los} and the escape velocity for a fixed R . We note that the assumption underlying the functional form of both $f_{\text{los}}(R, v_{\text{los}})$ and $f(E, L)$ is spherical symmetry and the state of equilibrium.

In our analysis we adopted the model of the distribution function proposed by Wojtak et al. (2008). The model was adjusted to the phase-space properties of dark matter particles in cluster-size haloes formed in cosmological N -body simulations. It assumes separability in the energy and the angular momentum, i.e. $f(E, L) = f_E(E)f_L(L)$, in which the angular momentum part is expressed by the following analytical ansatz

$$f(L) = \left(1 + \frac{L^2}{2L_0^2}\right)^{-\beta_\infty + \beta_0} L^{-2\beta_0}. \quad (2)$$

β_0 and β_∞ in (2) are two asymptotic values of the anisotropy parameter

$$\beta(r) = 1 - \frac{\sigma_\theta^2(r)}{\sigma_r^2(r)} \quad (3)$$

describing a ratio of the radial σ_r to tangential σ_θ velocity dispersion. The profile of the anisotropy is a monotonic function changing from β_0 at the cluster centre to β_∞ for large radii (see Wojtak et al. 2008). The scale of transition between these two asymptotes is specified by parameter L_0 .

The energy part $f_E(E)$ is given by the integral equation defining the relation between the distribution function and the assumed density profile of a tracer $\rho(r)$

$$\rho(r) = \iiint f_E(E) \left(1 + \frac{L^2}{2L_0^2}\right)^{-\beta_\infty + \beta_0} L^{-2\beta_0} d^3v. \quad (4)$$

This equation can be simplified to the form of a one-dimensional integral and solved numerically for $f_E(E)$ (see Appendix B in Wojtak et al. (2008)). In the following, we approximate the total density distribution by the universal NFW profile (Navarro et al. 1997), i.e.

$$\rho(r/r_s) = \frac{1}{4\pi(\ln 2 - 1/2)} \frac{1}{(r/r_s)(1 + r/r_s)^2} \frac{M_s}{r_s^3}, \quad (5)$$

where r_s is the scale radius and M_s is the mass enclosed in a sphere of this radius. We also assume that galaxies trace dark matter. This assumption, commonly referred to as a hypothesis of constant mass-to-number density profile, was shown to be fairly held for relatively large clustercentric radii (see e.g. Carlberg et al. 1997; Biviano & Girardi 2003). On the other hand, its robustness is more uncertain in the cluster centre: observations suggest that the profile of galaxy distribution at small radii may be as steep as dark matter (Lin, Mohr & Stanford 2004) or exhibit a core (Popesso et al. 2007). The problem of the consistency between the assumption about mass-to-number ratio and the data collected for our analysis is addressed in section 6.

Although M_s and r_s set the most natural scales for the phase-space units and both are used as the primary parameters of the mass profile in our analysis, a common way to parametrize the universal mass profile is to use the virial mass M_v and the concentration parameter c defined by equations

$$\begin{aligned} \frac{M_v}{(4/3)\pi r_v^3} &= \Delta_c \rho_c \\ c &= r_v/r_s, \end{aligned} \quad (6)$$

where r_v is the virial radius, ρ_c is the present critical density and Δ_c is the virial overdensity. For the cosmological model assumed in this paper $\Delta_c = 102$ (Bryan & Norman 1998; Lokas & Hoffman 2001).

Constraints on the parameters of the mass and anisotropy profiles were determined by means of the analysis of the posterior probability with the MCMC technique. Following Wojtak et al. (2009) we used the likelihood function defined by

$$L \propto \prod_{i=1}^{N_{\text{mem}}} f_{\text{los}}(R_i, v_{\text{los},i} | M_s, r_s, \beta_0, \beta_\infty), \quad (7)$$

where i is the reference number of a galaxy. The projected phase-space density (1) was evaluated numerically using the algorithm of Gaussian quadrature, as outlined in Wojtak et al. (2009). We note that f_{los} preserves the normalization within the aperture R_{\max} fixed in subsection 2.3. For the scale parameters we used the Jeffreys priors, i.e. $p(r_s) \propto 1/r_s$ and $p(M_s) \propto 1/M_s$. In order to assign equal weights for all types of the orbital anisotropy we adopted $\beta \rightarrow (-1/2) \ln(1 - \beta) = \ln(\sigma_r/\sigma_\theta)$ reparametrization and assumed flat priors for redefined parameters of the anisotropy profile. We fixed the value of L_0 parameter at $0.45r_s\sqrt{GM_s/r_s}$ which corresponds to $\sim 1r_s$ scale of the transition between β_0 and β_∞ , as found for massive dark matter haloes from cosmological simulations (see Wojtak et al. 2008). In order to keep positivity of the phase-space density in the cluster centre we narrowed the range of the prior for the central anisotropy to $\beta_0 \leq 1/2$ (An & Evans 2006). We also placed an upper limit on the outer anisotropy, $\beta_\infty = 0.99$, which solves the problem of an improper posterior distribution for models with $\beta_\infty \approx 1$.

We determined the Markov chains using the Metropolis-Hastings algorithm (see Gregory 2005; Wojtak et al. 2009). All free parameters of the algorithm were properly adjusted to keep the acceptance rate (the probability of parameter change between each two neighbouring models of the Markov chain) at the level of ~ 30 per cent which is the recommended value for many-parameters models (Gelman et al. 2004). Our Markov chains consist of 2×10^4 models. We checked that this length is sufficient to properly explore our parameter space, also in a joint modelling described in subsection 4.5. The convergence of the MCMC algorithm has been tested by means of monitoring the profile of the posterior probability along the chains, the analysis of the autocorrelation functions calculated for all parameters in use and the comparison of the parameter dispersions evaluated in different sections of the Markov chains. In this approach, properly mixed Markov chain is characterized by the posterior probability fluctuating around a flat profile, fast decay of the autocorrelation functions and possibly small variations of the parameter dispersions.

4 RESULTS OF THE ANALYSIS

We analyzed velocity diagrams of 41 nearby galaxy clusters in terms of the projected phase-space density, as described in section 3. Fig. 1 shows an example of the results obtained for the richest velocity diagram of the A1060 galaxy cluster. The contours show the 1σ and 2σ credibility constraints on

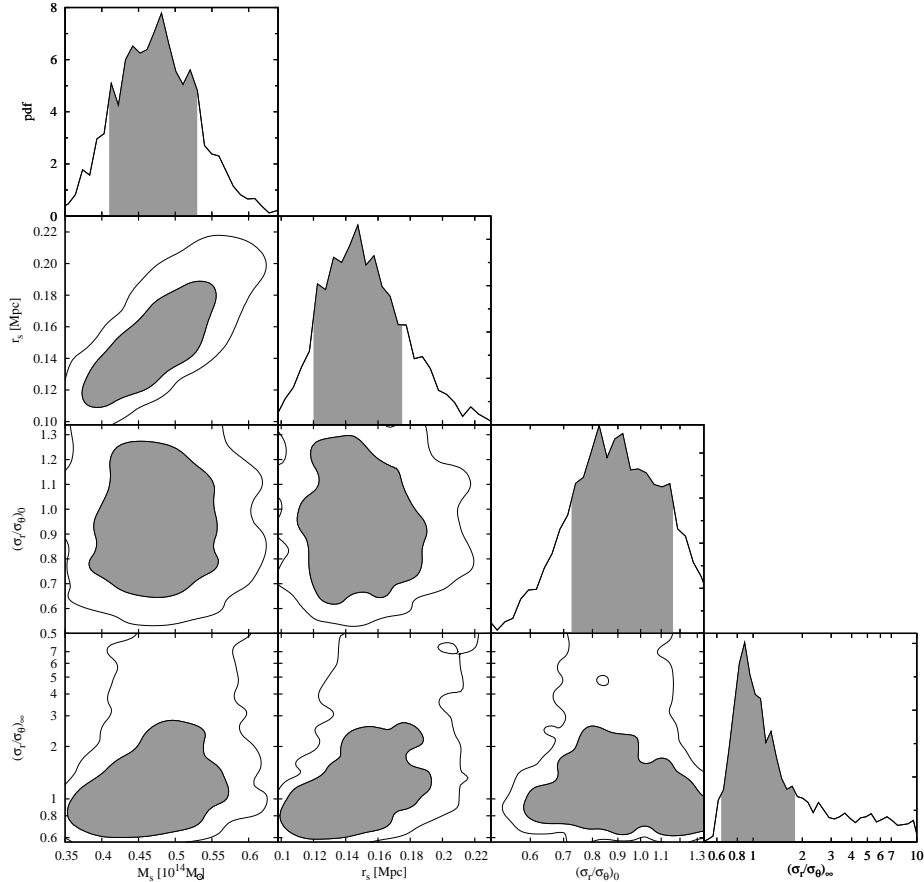


Figure 1. Results of the MCMC analysis of the velocity diagram for the A1060 galaxy cluster. Black solid lines are the contours of the 1σ and 2σ credibility areas (panels below the diagonal) or the profiles of the marginal probability distribution (panels along the diagonal). Gray areas indicate the 1σ credibility ranges of the parameters.

the parameters of the mass profile, M_s and r_s , and the profile of the orbital anisotropy, β_0 and β_∞ . The panels along the diagonal and in the top right corner show the profiles of the marginal probability distribution and indicate the 1σ credibility range for all parameters in use. We note that the 1σ and 2σ credibility ranges or contours are defined as those containing respectively 68 or 95 per cent of the corresponding marginal probability.

To save space we do not show graphical representations of the results for other clusters. Instead, in Table 2 we list numerical constraints on the parameters in the form of MAP (maximum a posteriori) values and the 1σ credibility ranges. Apart from the primary parameters of the mass profile used in our analysis, i.e. M_s and r_s , Table 2 also shows constraints on the virial mass M_v and the concentration parameter c .

Since our model of the distribution function is well-defined only within the virial sphere, we decided to replace the parameter β_∞ with β_{r_v} which is the anisotropy at the virial radius evaluated from the MAP value of the corresponding virial mass. The main motivation for this parameter replacement is to avoid the problem of the extrapolation of our model beyond the virial sphere. The new parameter of the orbital anisotropy was calculated using formulae for the velocity dispersions outlined in Wojtak et al. (2009). The errors were evaluated by propagating the 1σ limits for

the asymptotic values of the anisotropy profile to the virial radius. The final constraints on the anisotropy parameters are summarized in Table 2 in terms of a commonly used anisotropy parameter, β , as well as in terms of the ratio of the radial-to-tangential velocity dispersion, σ_r/σ_θ .

4.1 Scaling parameters of the mass profile

Fig. 2 shows the constraints on the scale radius r_s and the scale mass M_s , as listed in Table 2. Both parameters exhibit a clear correlation which may be attributed mostly to the presence of a typical scale of the overdensity inside the sphere of the scale radius or, equivalently, to a typical value of the concentration parameter. In order to show this property more explicitly we plotted the line of constant c equal to 7 which is the median value of the concentration parameter for the clusters (see Fig. 3). This concentration parameter corresponds to the mean density inside the sphere of scale radius equal to $\sim 5600\rho_c$.

Parameters of individual clusters are scattered around the line of the mean overdensity. This scatter is also shown in the form of the distribution of the concentration parameter (see Fig. 3). Interestingly, clusters with well-confirmed cool cores as well as clusters of early morphological type tend to populate the left part of the diagram in Fig. 2. This

cluster	$M_s [10^{14} M_\odot]$	$r_s [\text{Mpc}]$	$M_V [10^{14} M_\odot]$	c	$(\sigma_r/\sigma_\theta)_0$	$(\sigma_r/\sigma_\theta)_{r_V}$	β_0	β_{r_V}
A0085	2.81 ^{+0.53} _{-0.30}	0.65 ^{+0.16} _{-0.14}	12.33 ^{+1.78} _{-1.34}	4.25 ^{+0.76} _{-0.96}	1.16 ^{+0.16} _{-0.12}	2.04 ^{+0.12} _{-0.25}	0.26 ^{+0.17} _{-0.18}	0.76 ^{+0.03} _{-0.07}
A0119	1.08 ^{+0.24} _{-0.24}	0.45 ^{+0.11} _{-0.09}	5.05 ^{+0.73} _{-0.75}	4.61 ^{+0.79} _{-1.24}	1.16 ^{+0.17} _{-0.13}	2.06 ^{+0.13} _{-0.24}	0.26 ^{+0.18} _{-0.20}	0.76 ^{+0.03} _{-0.07}
A0133	0.69 ^{+0.28} _{-0.13}	0.19 ^{+0.10} _{-0.05}	5.69 ^{+1.47} _{-1.11}	11.27 ^{+1.49} _{-5.68}	1.22 ^{+0.13} _{-0.43}	0.94 ^{+1.36} _{-0.25}	0.33 ^{+0.13} _{-0.93}	-0.14 ^{+0.95} _{-0.95}
A0262	0.32 ^{+0.08} _{-0.30}	0.16 ^{+0.04} _{-0.04}	2.51 ^{+0.43} _{-1.23}	10.47 ^{+2.52} _{-1.89}	1.02 ^{+0.09} _{-0.50}	0.55 ^{+0.21} _{-0.15}	0.04 ^{+0.14} _{-0.22}	-2.26 ^{+1.54} _{-2.76}
A0376	0.80 ^{+0.12} _{-0.15}	0.25 ^{+0.08} _{-0.08}	5.56 ^{+1.53} _{-0.91}	8.35 ^{+1.91} _{-3.16}	0.71 ^{+0.28} _{-0.19}	1.89 ^{+0.37} _{-0.45}	-1.00 ^{+0.97} _{-1.71}	0.72 ^{+0.05} _{-0.20}
A0496	0.99 ^{+0.15} _{-0.11}	0.42 ^{+0.08} _{-0.07}	4.74 ^{+0.70} _{-0.58}	4.78 ^{+0.63} _{-1.02}	0.70 ^{+0.17} _{-0.11}	1.48 ^{+0.37} _{-0.32}	-1.04 ^{+0.72} _{-0.86}	0.54 ^{+0.16} _{-0.29}
A0539	0.42 ^{+0.09} _{-0.06}	0.14 ^{+0.05} _{-0.03}	3.75 ^{+0.57} _{-0.53}	12.89 ^{+1.66} _{-4.67}	0.92 ^{+0.24} _{-0.16}	2.19 ^{+0.16} _{-0.26}	-0.18 ^{+0.44} _{-0.54}	0.79 ^{+0.03} _{-0.06}
A0576	1.71 ^{+0.29} _{-0.18}	0.51 ^{+0.11} _{-0.10}	8.18 ^{+1.31} _{-1.02}	4.77 ^{+0.83} _{-1.24}	0.95 ^{+0.28} _{-0.15}	1.91 ^{+0.21} _{-0.25}	-0.12 ^{+0.45} _{-0.48}	0.72 ^{+0.05} _{-0.09}
A0671	0.58 ^{+0.24} _{-0.08}	0.14 ^{+0.06} _{-0.03}	5.55 ^{+1.01} _{-0.79}	15.51 ^{+1.48} _{-6.06}	0.66 ^{+0.31} _{-0.10}	1.24 ^{+0.92} _{-0.46}	-1.30 ^{+1.23} _{-0.86}	0.35 ^{+0.44} _{-0.99}
A0779	0.29 ^{+0.04} _{-0.04}	0.24 ^{+0.05} _{-0.05}	1.59 ^{+0.30} _{-0.18}	5.84 ^{+1.98} _{-1.98}	1.14 ^{+0.17} _{-0.18}	2.11 ^{+0.19} _{-0.39}	0.23 ^{+0.19} _{-0.32}	0.78 ^{+0.11} _{-0.11}
A0954	1.02 ^{+0.38} _{-0.29}	0.39 ^{+0.15} _{-0.12}	5.37 ^{+1.64} _{-1.18}	5.43 ^{+1.61} _{-2.01}	0.53 ^{+0.23} _{-0.10}	1.57 ^{+0.22} _{-0.47}	-2.58 ^{+1.83} _{-1.92}	0.59 ^{+0.10} _{-0.42}
A0957	0.40 ^{+0.11} _{-0.07}	0.14 ^{+0.05} _{-0.03}	3.58 ^{+0.54} _{-0.54}	13.01 ^{+1.75} _{-4.54}	0.81 ^{+0.37} _{-0.15}	1.29 ^{+1.02} _{-0.41}	-0.51 ^{+0.79} _{-0.79}	0.40 ^{+0.41} _{-0.67}
A0978	0.96 ^{+0.32} _{-0.14}	0.36 ^{+0.14} _{-0.11}	5.23 ^{+1.35} _{-0.84}	5.71 ^{+1.15} _{-2.43}	0.82 ^{+0.28} _{-0.24}	1.87 ^{+0.22} _{-0.49}	-0.48 ^{+0.66} _{-1.45}	0.71 ^{+0.06} _{-0.24}
A1060	0.45 ^{+0.08} _{-0.14}	0.14 ^{+0.04} _{-0.01}	4.10 ^{+0.39} _{-0.36}	13.99 ^{+1.22} _{-3.31}	0.90 ^{+0.25} _{-0.38}	0.88 ^{+0.77} _{-0.22}	-0.23 ^{+0.48} _{-0.72}	-0.28 ^{+0.92} _{-0.07}
A1139	0.41 ^{+0.05} _{-0.33}	0.39 ^{+0.17} _{-0.08}	1.57 ^{+1.82} _{-0.34}	3.53 ^{+1.25} _{-1.25}	0.87 ^{+0.38} _{-0.19}	1.75 ^{+0.56} _{-0.28}	-0.31 ^{+0.56} _{-0.83}	0.67 ^{+0.07} _{-0.14}
A1190	1.08 ^{+0.33} _{-0.19}	0.50 ^{+0.13} _{-0.13}	4.53 ^{+0.60} _{-1.07}	4.00 ^{+0.60} _{-1.65}	1.30 ^{+0.10} _{-0.36}	1.63 ^{+0.16} _{-0.16}	0.41 ^{+0.08} _{-0.52}	0.62 ^{+0.17} _{-0.09}
A1314	0.49 ^{+0.11} _{-0.07}	0.21 ^{+0.06} _{-0.05}	3.48 ^{+0.62} _{-0.47}	8.64 ^{+1.44} _{-2.69}	0.87 ^{+0.27} _{-0.21}	2.03 ^{+0.19} _{-0.44}	-0.33 ^{+0.55} _{-0.99}	0.76 ^{+0.04} _{-0.15}
A1650	2.52 ^{+0.69} _{-0.40}	0.82 ^{+0.29} _{-0.14}	8.19 ^{+1.48} _{-1.69}	2.95 ^{+0.35} _{-1.02}	1.17 ^{+0.17} _{-0.18}	1.56 ^{+0.48} _{-0.26}	0.27 ^{+0.17} _{-0.28}	0.59 ^{+0.17} _{-0.18}
A1691	1.38 ^{+0.54} _{-0.35}	0.58 ^{+0.25} _{-0.17}	5.36 ^{+1.69} _{-1.02}	3.64 ^{+0.92} _{-1.58}	0.92 ^{+0.35} _{-0.17}	1.77 ^{+0.29} _{-0.46}	-0.18 ^{+0.56} _{-0.60}	0.68 ^{+0.08} _{-0.26}
A1767	2.24 ^{+0.46} _{-0.46}	0.50 ^{+0.07} _{-0.13}	11.84 ^{+3.60} _{-3.40}	5.45 ^{+2.51} _{-2.30}	1.20 ^{+0.46} _{-0.31}	0.78 ^{+0.23} _{-0.15}	0.30 ^{+0.07} _{-0.15}	-0.66 ^{+1.39} _{-1.68}
A1773	1.23 ^{+0.33} _{-0.26}	0.42 ^{+0.13} _{-0.14}	6.33 ^{+1.41} _{-1.10}	5.24 ^{+1.59} _{-1.77}	1.11 ^{+0.25} _{-0.21}	2.06 ^{+0.18} _{-0.34}	0.19 ^{+0.27} _{-0.42}	0.76 ^{+0.04} _{-0.10}
A1795	1.01 ^{+0.25} _{-0.21}	0.23 ^{+0.09} _{-0.05}	8.04 ^{+1.25} _{-1.10}	10.51 ^{+1.27} _{-3.64}	1.31 ^{+0.09} _{-0.35}	0.51 ^{+0.23} _{-0.13}	0.42 ^{+0.07} _{-0.50}	-2.79 ^{+2.00} _{-2.87}
A1809	0.68 ^{+0.21} _{-0.14}	0.22 ^{+0.10} _{-0.04}	4.99 ^{+0.91} _{-0.65}	9.20 ^{+0.97} _{-3.20}	0.91 ^{+0.35} _{-0.31}	0.50 ^{+0.25} _{-0.12}	-0.21 ^{+0.59} _{-1.63}	-2.94 ^{+2.16} _{-2.80}
A1983	0.31 ^{+0.09} _{-0.05}	0.29 ^{+0.12} _{-0.07}	1.51 ^{+0.36} _{-0.33}	4.79 ^{+0.94} _{-2.01}	1.08 ^{+0.32} _{-0.23}	1.61 ^{+0.63} _{-0.23}	0.14 ^{+0.35} _{-0.52}	0.61 ^{+0.19} _{-0.14}
A2052	0.33 ^{+0.23} _{-0.05}	0.14 ^{+0.05} _{-0.04}	2.87 ^{+1.40} _{-0.49}	12.37 ^{+4.84} _{-1.40}	1.06 ^{+0.23} _{-0.21}	2.27 ^{+0.52} _{-0.52}	0.11 ^{+0.37} _{-0.49}	0.81 ^{+0.13} _{-0.13}
A2063	0.60 ^{+0.23} _{-0.08}	0.13 ^{+0.05} _{-0.03}	5.95 ^{+1.19} _{-0.77}	16.15 ^{+5.72} _{-5.72}	0.67 ^{+0.39} _{-0.17}	0.60 ^{+0.29} _{-0.18}	-1.20 ^{+1.31} _{-1.79}	-1.79 ^{+1.52} _{-2.86}
A2107	0.29 ^{+0.11} _{-0.03}	0.11 ^{+0.05} _{-0.03}	2.77 ^{+0.63} _{-0.44}	15.53 ^{+2.10} _{-6.23}	1.15 ^{+0.15} _{-0.34}	0.98 ^{+1.42} _{-0.22}	0.25 ^{+0.17} _{-0.78}	-0.05 ^{+0.87} _{-0.71}
A2142	4.93 ^{+1.46} _{-0.81}	0.99 ^{+0.31} _{-0.21}	16.70 ^{+2.41} _{-2.81}	3.10 ^{+0.42} _{-1.08}	1.07 ^{+0.17} _{-0.19}	1.61 ^{+0.37} _{-0.34}	0.13 ^{+0.22} _{-0.41}	0.61 ^{+0.13} _{-0.23}
A2175	2.11 ^{+0.99} _{-0.43}	0.77 ^{+0.39} _{-0.22}	6.88 ^{+1.71} _{-1.82}	2.96 ^{+1.87} _{-1.67}	1.03 ^{+0.24} _{-0.32}	1.82 ^{+0.19} _{-0.35}	0.05 ^{+0.33} _{-0.63}	0.70 ^{+0.05} _{-0.14}
A2415	0.57 ^{+0.13} _{-0.13}	0.25 ^{+0.08} _{-0.08}	3.66 ^{+0.90} _{-0.58}	7.33 ^{+2.58} _{-2.58}	1.00 ^{+0.24} _{-0.24}	2.08 ^{+0.36} _{-0.36}	0.01 ^{+0.73} _{-0.73}	0.77 ^{+0.11} _{-0.11}
A2593	0.55 ^{+0.09} _{-0.08}	0.43 ^{+0.11} _{-0.09}	2.08 ^{+0.37} _{-0.27}	3.56 ^{+0.67} _{-1.05}	1.23 ^{+0.15} _{-0.13}	2.03 ^{+0.11} _{-0.25}	0.34 ^{+0.13} _{-0.17}	0.76 ^{+0.02} _{-0.07}
A2634	0.77 ^{+0.17} _{-0.10}	0.22 ^{+0.08} _{-0.03}	5.83 ^{+0.73} _{-0.87}	9.74 ^{+1.18} _{-2.68}	1.24 ^{+0.12} _{-0.38}	0.79 ^{+0.47} _{-0.20}	0.35 ^{+0.11} _{-0.70}	-0.59 ^{+0.96} _{-1.25}
A2670	0.87 ^{+0.24} _{-0.06}	0.16 ^{+0.06} _{-0.02}	8.30 ^{+1.09} _{-0.90}	15.21 ^{+1.33} _{-4.80}	1.17 ^{+0.14} _{-0.33}	0.82 ^{+0.92} _{-0.23}	0.27 ^{+0.15} _{-0.70}	-0.49 ^{+1.16} _{-1.43}
A2734	1.34 ^{+0.42} _{-0.26}	0.57 ^{+0.29} _{-0.07}	5.21 ^{+1.39} _{-1.87}	3.65 ^{+0.14} _{-1.66}	0.66 ^{+0.20} _{-0.16}	0.92 ^{+0.78} _{-0.29}	-1.28 ^{+0.93} _{-1.75}	-0.19 ^{+0.84} _{-1.33}
A3158	1.56 ^{+0.52} _{-0.17}	0.25 ^{+0.10} _{-0.04}	12.93 ^{+2.45} _{-1.89}	11.47 ^{+1.41} _{-3.71}	0.83 ^{+0.41} _{-0.30}	0.72 ^{+0.51} _{-0.34}	-0.44 ^{+0.31} _{-2.05}	-0.92 ^{+1.14} _{-4.82}
A3571	1.36 ^{+0.26} _{-0.24}	0.25 ^{+0.07} _{-0.05}	10.83 ^{+1.20} _{-1.85}	10.62 ^{+1.92} _{-3.18}	1.09 ^{+0.98} _{-0.28}	1.35 ^{+0.22} _{-0.35}	0.16 ^{+0.22} _{-0.66}	0.45 ^{+0.36} _{-0.46}
A3581	0.21 ^{+0.10} _{-0.02}	0.12 ^{+0.07} _{-0.03}	1.77 ^{+0.43} _{-0.31}	12.25 ^{+1.09} _{-6.07}	0.90 ^{+0.36} _{-0.15}	1.14 ^{+1.18} _{-0.22}	-0.23 ^{+0.61} _{-0.52}	0.23 ^{+0.58} _{-0.40}
A3809	0.60 ^{+0.25} _{-0.08}	0.45 ^{+0.17} _{-0.13}	2.26 ^{+0.59} _{-0.50}	3.52 ^{+0.77} _{-1.48}	0.92 ^{+0.35} _{-0.21}	1.78 ^{+0.27} _{-0.34}	-0.19 ^{+0.57} _{-0.81}	0.69 ^{+0.08} _{-0.17}
A4059	1.16 ^{+0.23} _{-0.15}	0.55 ^{+0.15} _{-0.09}	4.45 ^{+0.63} _{-0.62}	3.57 ^{+0.68} _{-0.96}	0.84 ^{+0.29} _{-0.19}	1.72 ^{+0.24} _{-0.17}	-0.43 ^{+0.65} _{-0.53}	0.66 ^{+0.08} _{-0.08}
AS805	0.39 ^{+0.08} _{-0.05}	0.19 ^{+0.05} _{-0.05}	2.79 ^{+0.39} _{-0.40}	8.86 ^{+3.04} _{-3.04}	1.05 ^{+0.21} _{-0.18}	2.17 ^{+0.35} _{-0.44}	0.09 ^{+0.28} _{-0.44}	0.79 ^{+0.09} _{-0.09}
MKW4	0.23 ^{+0.05} _{-0.03}	0.14 ^{+0.05} _{-0.03}	1.81 ^{+0.27} _{-0.25}	10.43 ^{+1.38} _{-3.63}	1.06 ^{+0.20} _{-0.22}	2.23 ^{+0.13} _{-0.36}	0.11 ^{+0.25} _{-0.51}	0.80 ^{+0.02} _{-0.08}

Table 2. Constraints on the parameters of the mass and anisotropy profile of 41 galaxy clusters from the MCMC analysis of their velocity diagrams. The table provides the MAP values and the ranges containing 68 per cent of the corresponding marginal probability.

means that the clusters which are dynamically more evolved exhibit higher central overdensity (or higher concentration parameter). This property is also well-seen in Fig. 3, where we plotted the relative number of both types of clusters in subsequent bins of the concentration parameter. Cool core clusters (early type clusters) contribute 70 (60) per cent to the number of clusters with the concentration above the median value and 40 (30) per cent to the number of clusters below the median value. Although the effect is not prominent, we can conclude that clusters with high concentrations are more likely to be dynamically more evolved than clusters with less concentrated mass distribution.

The correlation between the state of dynamical evolution of clusters and the steepness of the mass profile shown in Figs. 2 and 3 is in agreement with the results of recent

cosmological simulations which point to two main factors responsible for this effect. First, more evolved clusters have not experienced severe mergers in their recent history and therefore tend to possess dark matter haloes with a steeper density profile (see e.g. Macciò et al. 2008). Second, quiescent phase in the recent formation history of these clusters likely leads to the survival of cool cores (see e.g. Burns et al. 2008; Hudson et al. 2010) and triggers the accumulation of baryonic gas due to the process of radiative cooling (see e.g. Gnedin et al. 2004). Higher concentration of gas in cluster centres deepens the gravitational potential well and consequently makes the density profile of dark matter steeper (see e.g. Dolag et al. 2009; Duffy et al. 2010).

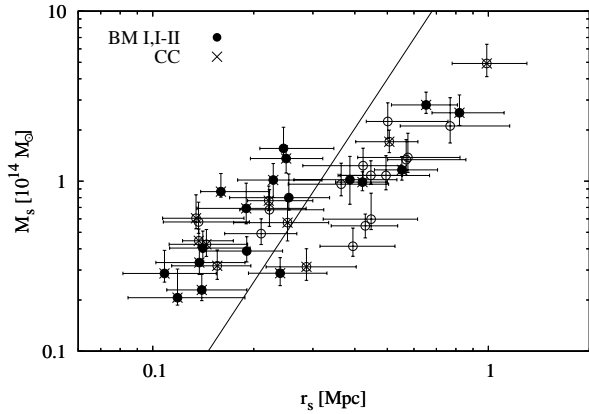


Figure 2. Parameters of the mass profile obtained from the MCMC analysis of 41 galaxy clusters, as listed in Table 2. Filled circles and crosses indicate early type (I,I-II type in Bautz-Morgan classification) clusters and cool core clusters. The solid line represents a family of density profiles with $c = 7$ which is the median value of the concentration parameter in the cluster sample.

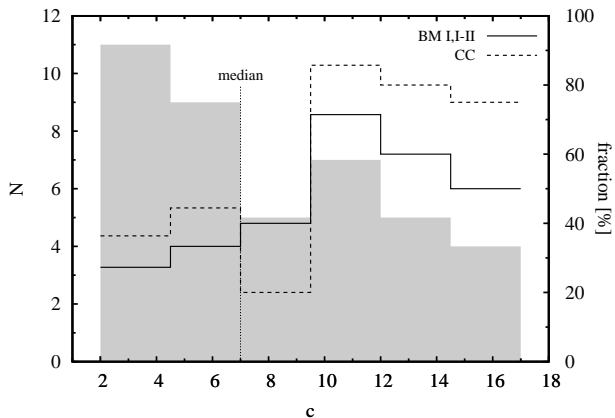


Figure 3. The distribution of the concentration parameter from Table 2 (shaded area). Dashed and solid lines show the relative numbers (right axis) of the cool core and early type (I, I-II type in Bautz-Morgan classification) clusters, respectively.

4.2 The mass-concentration relation

The concentration parameter and the virial mass are weakly anticorrelated (Navarro et al. 1997; Bullock et al. 2001). This relation reflects the mass assembly histories of dark matter haloes and may be used as an independent test of cosmological models. Here we use our constraints on the virial mass and the concentration parameter to test theoretical mass-concentration relation against observations in the mass regime of galaxy clusters.

Fig. 4 shows our estimates of the virial mass M_v and the concentration parameter c . According to the results of cosmological simulations the scatter of the concentration parameter may be effectively modelled by a lognormal distribution (Bullock et al. 2001; Macciò et al. 2008). The mean value of this distribution weakly varies as a power-law function of the virial mass, whereas the logarithmic dispersion

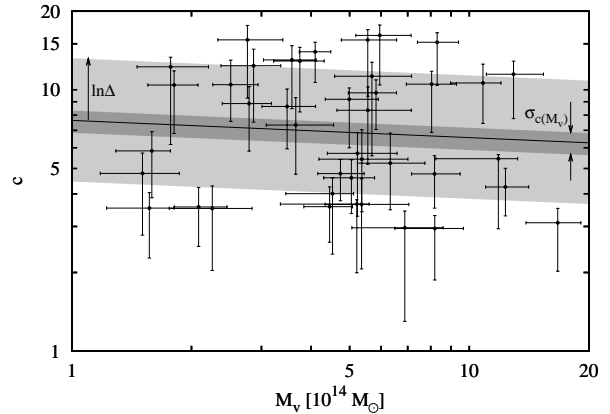


Figure 4. The mass-concentration relation from the analysis of 41 galaxy clusters. The solid line shows the best fit power-law profile for the mean concentration parameter. Shading indicates logarithmic dispersion of the concentration distribution, $\ln \Delta$, and the error of the normalization of the mean mass-concentration relation, $\sigma_{c(M_v)}$.

in the mass range of galaxy clusters is statistically consistent with being constant (Neto et al. 2007). This means that the distribution of clusters on the mass-concentration diagram may be described by the following probability density function (Comerford & Natarajan 2007)

$$f(c)dc = \frac{1}{\sqrt{2\pi c \ln \Delta}} \exp \left[\frac{-(\ln c - \ln \mu)^2}{2(\ln \Delta)^2} \right] dc, \quad (8)$$

where $\mu = c(M_0)(M_v/M_0)^\alpha$. In order to minimize the correlation between the slope and the normalization, the reference mass M_0 should be approximately the median value of the virial mass in the sample. In our case we assumed $M_0 = 5 \times 10^{14} M_\odot$.

We carried out the likelihood analysis of the data shown in Fig. 4. The likelihood function was the product of the probability density function (8) evaluated at the mass parameters of all clusters. The analysis was performed with the MCMC technique with three free parameters: the slope α , the normalization $c(5 \times 10^{14} M_\odot)$ and the logarithmic dispersion $\ln \Delta$. We note that the latter parameter includes both the internal scatter of the theoretical mass-concentration relation and the inaccuracy of the measurement of the concentration parameter.

Fig. 5 shows the constraints on the slope and the normalization of the mass-concentration relation. Three contours correspond to the 1σ , 2σ and 3σ credibility regions. Empty symbols with error bars indicate the constraints on the slope and the normalization of the $M_v - c$ relation obtained by Buote et al. (2007) from the analysis of X-ray clusters and by Comerford & Natarajan (2007) from the analysis of the mass parameters of galaxy clusters compiled from the literature. In both cases, the original results were properly adapted to the overdensity parameter assumed in our work as well as to the reference mass M_0 . Our result agrees within errors with the constraints obtained by Buote et al. (2007) and Comerford & Natarajan (2007), although clearly a lower value of the normalization is preferred, $c(5 \times 10^{14} M_\odot) = 6.9_{-0.7}^{+0.6}$.

In order to compare our results with theoretical pre-

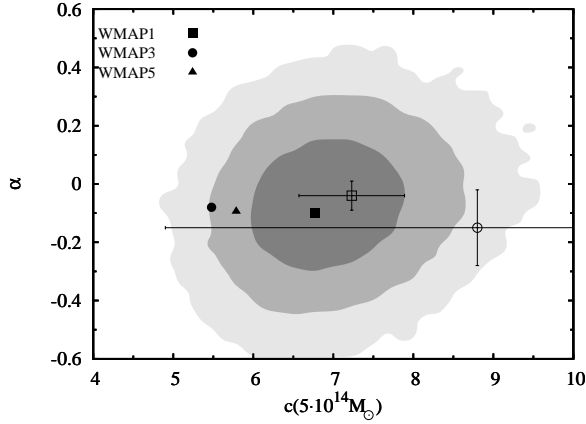


Figure 5. Constraints on the parameters of the power-law fit to the mass-concentration data, the slope α and the normalization at the mass $5 \times 10^{14} M_{\odot}$. The empty square and circle with error bars show the constraints on the parameters of the mass-concentration relation obtained by Buote et al. (2007) and Comerford & Natarajan (2007), respectively. Filled symbols indicate the calibrations of the mass-concentration relation from cosmological N -body simulations (see Macciò et al. 2008) with the parameters from three data releases of the WMAP satellite labelled by WMAP1, WMAP3 and WMAP5.

dictions we plotted in Fig. 5 the calibrations of the mass-concentration relation for relaxed dark matter haloes formed in cosmological N -body simulations (see Macciò et al. 2008), where an appropriate change of the virial overdensity parameter was taken into account. We note that the reference simulations are purely dark matter simulations which do not take into account the steepening of dark matter profile induced by baryonic gas (see Gnedin et al. 2004). To account for this effect we increased all normalizations by 10 per cent which is the value close to the upper limit of the bias in the concentration parameter found in hydrodynamical simulations of galaxy clusters (see Dolag et al. 2009; Duffy et al. 2010). Each calibration (filled points in Fig. 5) refers to one of three cosmological models given by the parameters from three data releases of the Wilkinson Microwave Anisotropy Probe (WMAP) satellite, WMAP1 (Spergel et al. 2003), WMAP3 (Spergel et al. 2007), and WMAP5 (Komatsu et al. 2009). The main difference between these three sets of cosmological parameters lies in the value of σ_8 , the linear amplitude of density perturbations at $8 h^{-1} \text{Mpc}$ scale at $z = 0$, which ranges from 0.75 for WMAP3, through 0.8 for WMAP5, to 0.9 for WMAP1. Keeping in mind that the normalization of the $M_v - c$ relation is mostly sensitive to σ_8 , the three values of σ_8 correspond to three normalizations labelled by WMAP1, WMAP3 and WMAP5 in Fig. 5. From Fig. 5 one can see that our constraints on the normalization of the mass-concentration relation are fully consistent with σ_8 of WMAP1 cosmology and agrees only at 2σ and $\sim 1\sigma$ level with that of WMAP3 and WMAP5, respectively. We confirm recent findings that the concentration parameters for galaxy clusters tend to be higher than those predicted by cosmological model with WMAP3 or WMAP5 parameters (see Buote et al. 2007; Duffy et al. 2008).

In order to place constraints on σ_8 using the lim-

its for the normalization $c(M_0)$ we adopted a semianalytical model for the mass-concentration relation proposed by Bullock et al. (2001). According to this model the mean concentration parameter at redshift $z = 0$ is inversely proportional to the scale factor a_c of halo collapse given by the following equation

$$\sigma(FM_v) = \frac{1.686}{D(a_c)}, \quad (9)$$

where $D(a)$ is the linear growth rate, σ is the present linear rms density fluctuation at the mass scale FM_v and F is a free parameter of this model. Assuming that the only factor determining the normalization $c(M_0)$ at a fixed virial mass M_0 is the value of σ_8 we find that $\sigma_8 \propto 1/D(a_c)$ and $c(M_0) \propto 1/a_c$. We used both proportionalities to convert $c(M_0)$ into σ_8 . In this conversion, we assumed the calibration from Macciò et al. (2008) for $\sigma_8 = 0.9$ and corrected for 10 per cent bias upwards, i.e. $c(5 \times 10^{14} M_{\odot}) = 6.8$ (see Fig. 5), where a_c was calculated using equation (9) with $F = 0.001$ which is the recommended value for the mass regime of galaxy clusters (Bullock et al. 2001; Buote et al. 2007). As a result we expressed the constraints on the mean mass-concentration relation in terms of σ_8 parameter obtaining $\sigma_8 = 0.91^{+0.07}_{-0.08}$. We note that the difference between WMAP value of σ_8 and its value from WMAP5 data release corresponds to the change of $c(M_0)$ by -14 per cent. We cannot exclude that this difference may arise from systematic errors in the measurement of the concentration parameter, observational selection biases or an insufficient value of the bias correcting the calibration of the mass-concentration relation for the presence of baryons.

Our constraint on the slope of the $M_v - c$ relation is rather weak, i.e. $\alpha = -0.07 \pm 0.15$. It is consistent with a flat profile as well as with the slope obtained in cosmological simulations ($\alpha \sim -0.1$). The best-fit value of the logarithmic dispersion parameter $\ln \Delta$ is 0.55. The width of the light gray region in Fig. 4 indicates this value, whereas the black solid line and the dark gray area show the best-fit profile for the mean concentration $\mu(M_v)$ and the error of the normalization. Taking into account that the statistical scatter in the measurement of the concentration parameter is around $\sigma_{\ln \Delta} \approx 0.44$ (see Wojtak et al. 2009), we conclude that the logarithmic dispersion of an intrinsic scatter in the theoretical $M_v - c$ relation is about 0.35 which is in fair agreement with the results of cosmological simulations (Bullock et al. 2001; Neto et al. 2007; Macciò et al. 2008).

4.3 Mass scaling relations

The virial mass of galaxy clusters scales with a number of different observables. Here we consider scaling relations with the velocity dispersion, the X-ray temperature and the X-ray luminosity (see Fig. 6). The virial mass, as listed in Table 2, comes from our analysis of 41 velocity diagrams of nearby galaxy clusters. Velocity dispersions were calculated using all galaxies lying within the virial radii of the clusters. The errors were estimated by bootstrapping from the sample. We used the same kinematic data as in the proper analysis of velocity diagrams. The temperatures were obtained by Horner (2001) from the spectral analysis of data acquired by the ASCA satellite (23 clusters). The luminosities were taken from the catalogues of X-ray clusters observed by the

relation	α	$M_0[10^{14}M_\odot]$
$M_v = M_0 \left[\sigma_{\text{los}} / (750 \text{ km s}^{-1}) \right]^\alpha$	3.17 ± 0.13	5.99 ± 0.17
$M_v = M_0 \left[L_X / (10^{44} \text{ erg s}^{-1}) \right]^\alpha$	0.49 ± 0.05	5.53 ± 0.33
$M_v = M_0 \left[T_X / (5 \text{ keV}) \right]^\alpha$	1.54 ± 0.12	7.85 ± 0.55

Table 3. Best-fit parameters of the power-law approximation for the three different mass scaling relations.

ROSAT satellite in the energy band 0.1–2.4 keV: the Northern ROSAT All-Sky (NORAS) galaxy cluster survey (see Böhringer et al. 2000), the ROSAT-ESO Flux Limited X-ray (REFLEX) galaxy cluster survey (see Böhringer et al. 2004) and a complementary source of the data provided by Ledlow et al. (2003). All luminosities were corrected for the assumed cosmological parameters.

All scaling relations seen in Fig. 6 are well approximated by a power-law function. Table 3 lists the best-fit slope and normalization for each of them. Parameters of the scaling relations were obtained by fitting a line to the data in logarithmic scales. We used symmetrized logarithmic errors given by $(x_2 - x_1)/(2x_0)$, where x_1 and x_2 are the boundaries of the 1σ credibility range of x variable, and x_0 is the most probable value. The best-fit slope and normalization were calculated using the bisector method (Isobe et al. 1990). The pivot points of σ_{los} , L_X and T_X given in Table 3 were taken to be approximately the median values of the corresponding variables. This minimized the correlation between the slope and normalization. The errors were evaluated by bootstrap resampling.

The best-fit scaling relations were plotted in Fig. 6. Solid lines are the best power-law fits and the shaded areas indicate the errors in both the slope and normalization. Both the temperature and the velocity dispersion appear to correlate very well with the virial mass. We note, however, that the a tight correlation with the velocity dispersion occurs mainly due to the fact that the virial masses were derived from the same kinematic data that were used to evaluate velocity dispersions. Two clusters, A119 and A2107, lie below the mean mass-temperature relation. This discrepancy is probably caused by the fact that these clusters are less relaxed compared to the other ones in our sample: A119 exhibits distinct substructuring (Schuecker et al. 2001), whereas A2107 has a high-velocity ($\sim 200 \text{ km s}^{-1}$) cD galaxy that may suggest some merging activity. The correlation between X-ray luminosities and the virial masses is weaker and confirms a well-known fact that the X-ray luminosity is not a robust mass proxy. Nevertheless, we note that our constraint on the slope of the $M_v - L_X$ relation is in fair agreement with other measurements available in the literature ranging between 0.5 and 0.7 (see e.g. Popesso et al. 2005; Lopes et al. 2009).

The slopes of the mass scaling relations with the X-ray temperature as well as with the velocity dispersion are fully consistent with the predictions of the virial theorem which states that $M_v \propto \sigma^3 \propto T_X^{3/2}$ (Bryan & Norman 1998). The slope of the mass-temperature relation is in excellent agreement with the most recent estimates which yield values between 1.5 and 1.6 (see e.g. Vikhlinin et al. 2006).

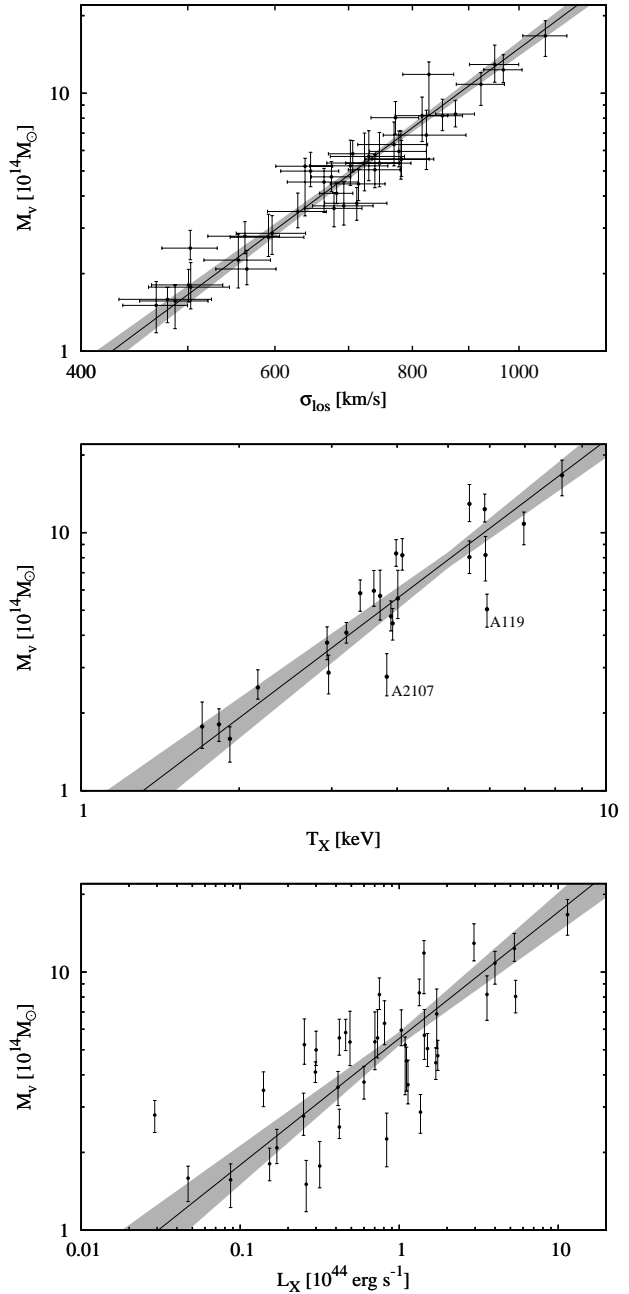


Figure 6. Scaling relations between the virial mass and different mass proxies: the velocity dispersion (σ_{los}), the X-ray luminosity (L_X) and the X-ray temperature (T_X). Solid lines show the best power-law fits and gray shaded areas represent the errors in both the slope and normalization.

The normalization of the same relation, when converted to the overdensity $\Delta_c = 500$, is $(4.7 \pm 0.3) \times 10^{14} M_\odot$ and agrees with that derived from high-resolution hydrodynamical simulations (see e.g. Borgani et al. 2004). It is consistent with the normalization of X-ray derived mass-temperature relation (see e.g. Arnaud, Pointecouteau & Pratt 2005; Vikhlinin et al. 2006) and is lower by ~ 20 per cent than mass-temperature normalization determined from weak lensing masses (see e.g. Pedersen & Dahle 2007).

Our analysis provides an independent test of the scaling

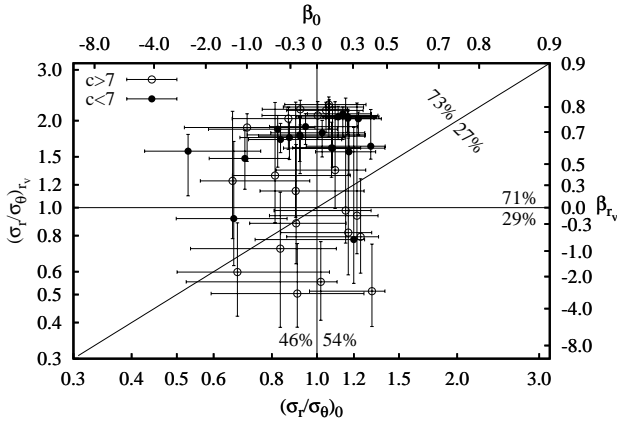


Figure 7. The orbital anisotropy of galaxies in 41 galaxy clusters. Empty and filled symbols refer to the clusters with the concentration parameter above or below the median concentration in the sample ($c = 7$). Numbers indicate fractions of clusters in domains of the diagram defined by the lines of isotropic velocity distribution ($\beta_0 = 0$ or $\beta_{r_v} = 0$) and the family of flat anisotropy profiles ($\beta_0 = \beta_{r_v}$).

relations with X-ray observables on the scale of the virial overdensity that is usually not used for X-ray clusters. Since X-ray flux is detected in the very central part of clusters, a typical scale of the mass probed in X-ray observations is between M_{200} and M_{500} . This mass scale is also commonly used to study X-ray scaling relations. Our analysis shows that the mass scaling relations both with T_X and L_X may be extended to the virial mass with the mean overdensity $\sim 100\rho_c$.

4.4 The anisotropy of galaxy orbits: individual clusters

Fig. 7 shows the constraints on the orbital anisotropy of galaxies in the cluster centre (β_0) and at the virial sphere (β_{r_v}). Although Wojtak et al. (2009) showed that the estimate of the anisotropy in the outer part of the cluster appears to be much less accurate than in the central part, we think that some interesting conclusions may be drawn from studying the overall distribution of the results obtained for individual clusters. The estimates of the central anisotropy for all clusters are statistically consistent with $\beta_0 = 0$. Galaxy orbits at the virial sphere of the clusters are noticeably radially biased with a typical anisotropy of around $(\sigma_r/\sigma_\theta)_{r_v} = 1.7$. We also note that there is a clear tendency of the anisotropy profile to increase with radius: over 70 per cent of the results lie above the line of flat anisotropy profiles indicated by the diagonal. On the other hand, some clusters exhibit flat β profile with an isotropic velocity dispersion tensor.

Clusters with different degrees of dark matter concentration tend to populate different regions of the parameter space shown in Fig. 7. In particular, low concentration clusters ($c < 7$) exhibit more radially biased galaxy orbits at the virial sphere than clusters with higher value of the concentration ($c > 7$). Furthermore, the former clusters seem to constitute a very homogeneous class in terms

of the anisotropy profile. The orbital anisotropy of galaxies in these clusters seems to grow with radius between two universal asymptotes: $\sigma_r/\sigma_\theta \approx 1$ in the cluster centre and $\sigma_r/\sigma_\theta \approx 1.8$ at the virial radius. In the case of the high concentration clusters, the anisotropy profiles do not show any signatures of such universality. The anisotropy at the virial radius in these clusters ranges from $(\sigma_r/\sigma_\theta)_{r_v} \sim 1$ to $(\sigma_r/\sigma_\theta)_{r_v} \sim 2$. Nevertheless, it is interesting to note that 85 per cent of the clusters for which constraints on the anisotropy parameters are statistically consistent with the fully isotropic model ($\beta_0 = \beta_{r_v} = 0$) are high concentration clusters.

Keeping in mind that the degree of mass concentration in galaxy clusters is related to the state of dynamical evolution, we suggest that the dichotomy between the low and high concentration clusters observed in Fig. 7 may be likely the result of the cluster evolution. In this scenario galaxy orbits of less evolved clusters (low concentration parameter) would be dominated by radial motions in their outer parts (filled symbols in Fig. 7), whereas for more evolved clusters galaxy orbits tend to be more isotropic both in the cluster centre as well as in the vicinity of the virial sphere.

At the early stage of cluster evolution one can expect an excess of radial orbits around the virial sphere. This excess is mostly the effect of radial infall of galaxies onto the clusters. Due to the relaxation process the initial orbits of infalling galaxies are expected to become more isotropic with time so that the most evolved clusters are characterized by more isotropic distribution of galaxy orbits. A similar mechanism of the isotropization of galaxy orbits in clusters was pointed out by Biviano & Katgert (2004). Studying the orbital structure in ENACS (ESO Nearby Abell Cluster Survey) clusters, Biviano & Katgert (2004) showed that early type galaxies (ellipticals) are characterized by more isotropic orbits than spirals for which σ_r/σ_θ at the virial sphere is around 1.7. Since the former galaxy population is more evolved and relaxed than the latter, this orbital segregation implies that a mechanism of the orbital isotropization must operate during cluster evolution.

4.5 The anisotropy of galaxy orbits: a joint analysis

In order to estimate the typical anisotropy profile of galaxy orbits in the clusters of our sample we carried out a joint MCMC analysis of all velocity diagrams. Following Wojtak et al. (2009) we defined the likelihood function as

$$f(M_{s,1}, \dots, M_{s,n}, r_{s,1}, \dots, r_{s,n}, \beta_0, \beta_\infty) = \prod_{j=1}^n \prod_{i=1}^{N_{\text{mem}}(j)} f_{\text{los}}(R_{j,i}, v_{\text{los},j,i} | \{M_{s,j}, r_{s,j}, \beta_0, \beta_\infty\}), \quad (10)$$

where j and i are respectively the reference numbers of a clusters and a galaxy of the j -th velocity diagram. The two parameters of the anisotropy profile, β_0 and β_∞ , are common to all clusters and define the anisotropy profile in cluster population, whereas parameters of the mass profile fix phase-space units for individual clusters. We used the constraints on the parameters of the mass profile, M_s and r_s , in the form of Gaussian prior, where the means and the dispersions were given by MAP values and symmetrized errors corresponding to the 1σ credibility ranges.

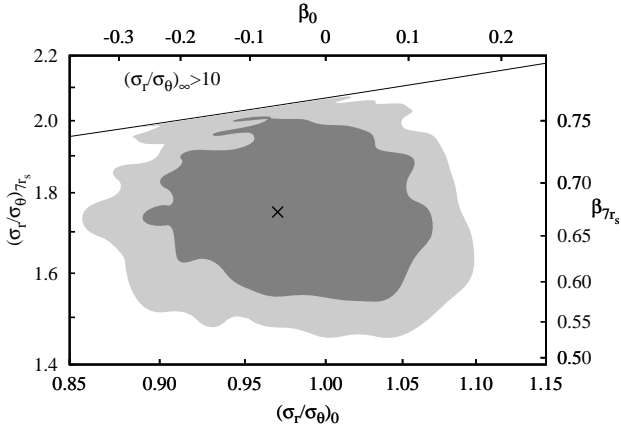


Figure 8. Constraints on the parameters of the anisotropy profile of galaxy orbits from the joint analysis of 41 nearby galaxy clusters. The gray shading shows the 1σ and 2σ confidence regions of the marginal probability distribution and the cross indicates the MAP value. The black solid line marks the boundary of the parameter space excluded from the analysis by the prior $(\sigma_r/\sigma_\theta)_\infty < 10$.

Fig. 8 shows the result of a joint analysis in the form of the 1σ and 2σ credibility contours of the marginal probability distribution. In order to avoid extrapolation beyond the virial sphere we converted β_∞ parameter into the anisotropy at $7r_s$ which is a typical scale of the virial radius in the cluster sample. The black solid line indicates the boundary of the parameter space excluded from the analysis by the prior $(\sigma_r/\sigma_\theta)_\infty < 10$. The joint analysis confirms that galaxy orbits are typically isotropic in the cluster centres, $(\sigma_r/\sigma_\theta)_0 = 0.97 \pm 0.04$, and radially anisotropic at the virial sphere, $(\sigma_r/\sigma_\theta)_{7r_s} = 1.75^{+0.23}_{-0.19}$. The degree of the anisotropy at the virial sphere agrees with the value of the orbital anisotropy determined for late type galaxies which dominate in the outer parts of galaxy clusters (Biviano & Katgert 2004). We do not confirm the result obtained by van der Marel et al. (2000) who concluded that velocity distribution in galaxy clusters is consistent with isotropic orbits. The reason of this discrepancy may lie in that fact that van der Marel et al. (2000) assumed a flat profile of the anisotropy. Taking into account that the central anisotropy is much better constrained than the anisotropy in the outer part of a cluster (Wojtak et al. 2009), one may expect that the estimate of the global anisotropy is dominated by its central rather than the outermost value.

The size of the credibility regions in Fig. 8 does not reflect the scatter of the anisotropy profiles in the cluster sample. It rather describes the accuracy of parameter estimation under the assumption that the cluster sample is homogeneous in terms of the anisotropy profile. In order to illustrate the degree of the internal scatter of the anisotropy parameters within our cluster sample we repeated the joint analysis for two separate cluster subsamples, clusters with the concentration parameters above ($c > 7$) and below ($c < 7$) the median (see Fig. 9). The choice of these subsamples is motivated by the observed segregation of low and high concentration clusters on the plane of the anisotropy param-

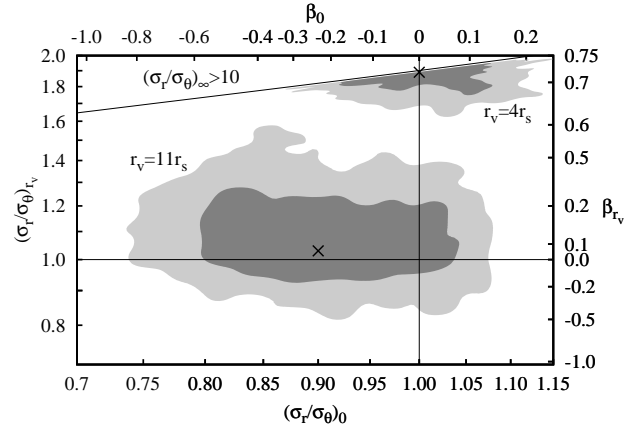


Figure 9. Constraints on the parameters of the anisotropy profile of galaxy orbits from the joint analysis of low concentration clusters (with $c < 7$ and the median virial radius $r_v \approx 4r_s$) and high concentration clusters (with $c > 7$ and the median virial radius $r_v \approx 11r_s$). The gray shading shows the 1σ and 2σ confidence regions of the marginal probability distribution and the crosses indicate the MAP values. The black solid line marks the boundary of the parameter space excluded from the analysis by the prior $(\sigma_r/\sigma_\theta)_\infty < 10$.

eters (see Fig. 7). Our result confirms the conclusion from the previous subsection that low concentration clusters have galaxies on clearly radially biased orbits at the virial sphere, whereas galaxy orbits for high concentration clusters tend to be isotropic at all radii within the virial sphere.

5 COMPARISON WITH OTHER METHODS

For a number of galaxy clusters parameters of the mass profile have already been determined with other methods. In this section, we use these estimates to compare with the results obtained with our method. This comparison allows us to check the credibility of our approach with respect to other methods of mass inference for galaxy clusters.

Fig. 10 shows the comparison between the virial mass estimated in our analysis and with other methods available for nearby galaxy clusters. The bottom panel includes the mass estimates obtained from the X-ray observations. It comprises both the results of a detailed analysis of the temperature profiles (Pointecouteau et al. 2005; Vikhlinin et al. 2006) and the mass estimates obtained under the assumption that the intracluster gas is isothermal (Reiprich & Böhringer 2002) or is linked to the temperature via a polytropic equation of state (Sanderson et al. 2003). The top panel presents the mass estimates from galaxy kinematics including the Jeans analysis with the velocity dispersion σ_{1os} and the kurtosis κ_{1os} (Łokas et al. 2006; Wojtak & Łokas 2007), and the caustic method (Rines et al. 2003; Rines & Diaferio 2006). We note that all mass estimates were adopted to the virial overdensity assumed in this work. In the conversion between masses corresponding to different overdensities, we used the same mass profile as assumed by the authors of a given data analysis. Apart from the analysis carried out by Reiprich & Böhringer (2002) and Sanderson et al. (2003) who used the mass profile derived

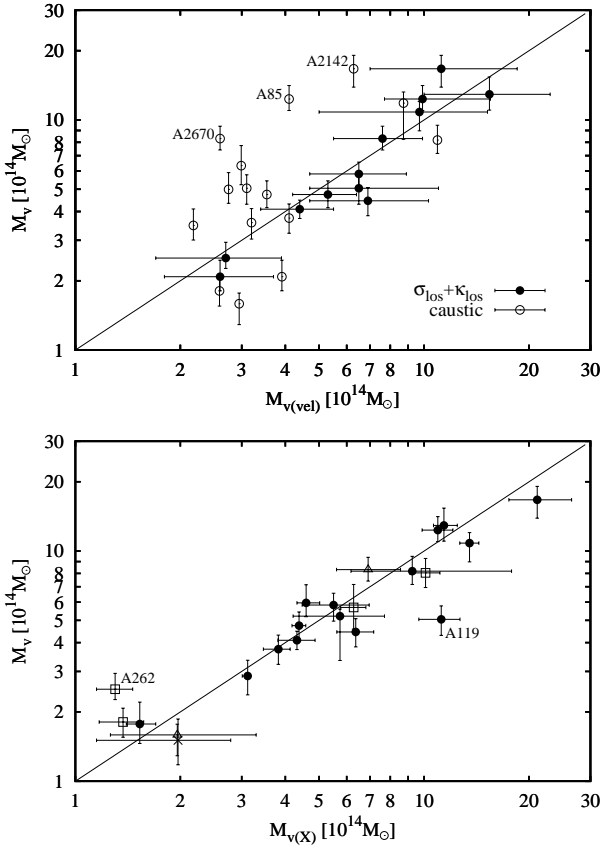


Figure 10. Comparison between the virial mass obtained with the method of the projected phase-space analysis (M_v) and other methods based on the X-ray observations ($M_{v(X)}$, bottom panel), the Jeans analysis of velocity moments and the caustic technique ($M_{v(vel)}$, top panel). The sources of data for subsequent point types are the following: filled circles in the top panel: Lokas et al. (2006); Wojtak & Lokas (2007); empty circles in the top panel: Rines et al. (2003); Rines & Diaferio (2006); filled circles in the bottom panel: Reiprich & Böhringer (2002); empty squares: Vikhlinin et al. (2006); empty triangle: Sanderson et al. (2003); cross: Pointecouteau et al. (2005). The black solid line represents equality between the mass estimates.

from the equation of hydrostatic equilibrium with a fixed parametrization of the gas density and the temperature profile, the mass profile was parametrized by the NFW formula (5).

Our mass determinations agree within errors with the estimates based on X-ray analysis. There are two clusters, A119 and A262, for which the difference between mass estimates exceeds significantly the 1σ level. The reason of this discrepancy seems to be clear for A119, since this is one of the least relaxed clusters of our sample (Schuecker et al. 2001). On the other hand, an analogous discrepancy for A262 remains unclear, since there is no observational evidence which would indicate that this cluster is not in equilibrium. We checked that both the X-ray mass and the mass inferred from galaxy kinematics, as displayed in Fig. 10, are consistent with the corresponding result obtained by independent authors (Lokas et al. 2006; Gastaldello et al. 2007). This suggests that this difference is probably a consequence of a generic tension between kinematic and X-ray data.

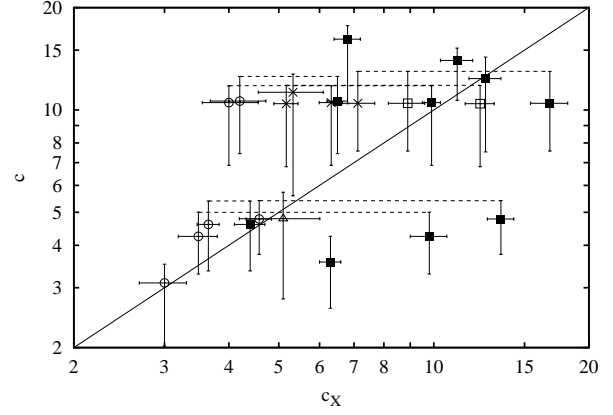


Figure 11. Comparison between the concentration parameter obtained with the method of the projected phase-space analysis (c) and from the X-ray observations (c_X). The sources of data for subsequent point types are the following: filled squares: Xu et al. (2001); empty squares: Gastaldello et al. (2007); crosses: Vikhlinin et al. (2006); circles: Ettori, De Grandi & Molendi (2002); triangle: Pointecouteau et al. (2005). The black solid line represents equality between both estimates of the concentration parameter. The dashed lines connect data for the same clusters.

The virial masses obtained in our work agree very well with those determined in the analysis of velocity moments. This fact is fully understandable, since our approach to data modelling is an extension of the formalism based on velocity moments. We note that the 1σ credibility ranges obtained with our method are noticeably narrower than those resulting from the Jeans analysis and are comparable to the errors of the X-ray masses.

The caustic method provides mass estimates which marginally agree with the virial masses determined with our approach. The caustic mass correlates with the virial mass from our analysis, but is considerably scattered around the line of equal mass estimates and tends to be underestimated with respect to our mass determination. For three cases, A85, A2142 and A2670, this effect is most prominent: the caustic virial mass is ~ 3 smaller than its counterpart from our analysis. We checked that our measurements of the virial masses for these clusters agree with the estimates from the X-ray observations yielding $\sim 1.1 \times 10^{15} M_\odot$ for A85 (Reiprich & Böhringer 2002; Durret, Lima & Forman 2005), $\sim 2.1 \times 10^{15} M_\odot$ for A2142 (Reiprich & Böhringer 2002) and $\sim 7 \times 10^{14} M_\odot$ for A2670 (Sanderson et al. 2003). This confirms that the caustic masses of these three clusters are likely underestimated.

Fig. 11 shows the comparison between the concentration parameters obtained with our method and from the X-ray observations of the corresponding clusters (see Xu et al. 2001; Ettori, De Grandi & Molendi 2002; Vikhlinin et al. 2006; Gastaldello et al. 2007). We note that some clusters (A85, A119, A262, A496, A1795, A3571 and MKW4) have multiple representations on this diagram corresponding to the estimates obtained by different authors. Since for some clusters these estimates do not agree within the errors, we decided to plot all results. The points referring to the same cluster were connected with a horizontal dashed line. As for the comparison of the virial masses, the concentration pa-

	1 Mpc	1.7 Mpc	r_v
M_s	0.001 ± 0.140	0.015 ± 0.056	0.017 ± 0.049
r_s	-0.030 ± 0.171	0.012 ± 0.094	0.020 ± 0.077
M_v	0.038 ± 0.173	-0.010 ± 0.101	-0.019 ± 0.082
c	0.025 ± 0.105	0.008 ± 0.042	0.003 ± 0.033
$(\sigma_r/\sigma_\theta)_0$	-0.035 ± 0.101	-0.008 ± 0.038	-0.003 ± 0.026
$(\sigma_r/\sigma_\theta)_\infty$	-0.112 ± 0.588	0.001 ± 0.253	-0.007 ± 0.219

Table 4. Statistics of the relative residuals of the model parameters from the analysis of 41 velocity diagrams with three different truncation radii, R_{\max} . Each row lists the means and dispersions in the cluster sample for the relative residuals defined by $\log(X_{R_{\max}}/X_{2.5\text{Mpc}})$, where $X_{R_{\max}}$ is the MAP value of the parameter obtained in the analysis of velocity diagrams truncated at R_{\max} .

parameters were properly converted to the virial overdensity assumed in this work.

The concentration parameter determined with our method correlates with that inferred from the X-ray data, although the scatter is significantly larger than for the virial mass. Assuming a power-law relation between both estimates, $c = c_7(c_X/7)^\alpha$, we obtained the following constraints on the slope and the normalization: $\alpha = 1.04 \pm 0.4$ and $c_7 = 8.2 \pm 1.0$, where the fit was performed in the same manner as described in subsection 3.3. Although the data sample is not statistically uniform so we cannot draw any firm conclusion, we point out that X-ray derived concentrations tend to be smaller by ~ 15 per cent than the concentrations inferred from galaxy kinematics.

6 SELF-CONSISTENCY TESTS

6.1 Completeness

An important factor that may influence the quality of our analysis is the completeness of spectroscopic data. In order to check this effect we carried out the following test. If the data are incomplete one may expect that the parameters estimated from velocity diagrams truncated at different projected radii will be different. To see if this is the case we repeated the analysis for all clusters with three different values of the maximum projected radius: $R_{\max} = 1$ Mpc, $R_{\max} = 1.7$ Mpc and $R_{\max} = r_v$, where r_v is the virial radius taken from the first analysis with $R_{\max} = 2.5$ Mpc. Table 4 shows the comparison between parameter estimates obtained for different sizes of the aperture. Each row contains the logarithmic mean and dispersion of the relative residuals for the MAP values, where the reference values of the parameters come from the analysis with $R_{\max} = 2.5$ Mpc (see Table 2).

We see that there is no trend in the mean value of the residuals. One may notice a negative bias in the outer asymptotic value of the anisotropy profile for $R_{\max} = 1$ Mpc. This is, however, a consequence of the fact that using a smaller aperture we probe the inner part of the clusters for which the orbits are more isotropic. We also note that the logarithmic dispersions which describe the scatter of the relative residuals are smaller or comparable to the relative errors associated with the 1σ credibility ranges listed in Table 2. This property together with the stability of the mean values means that our results are not sensitive to the change

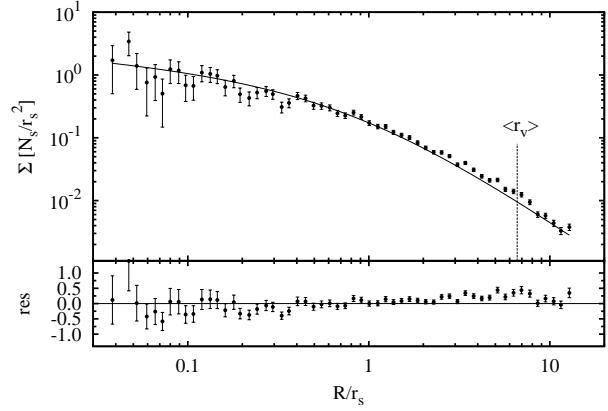


Figure 12. Surface number density of galaxies in 41 galaxy clusters combined into one. The black solid line is the projected NFW profile. The vertical line indicates a typical scale of the virial radius.

of the truncation radius of velocity diagrams. This excludes the possibility that the data may be subject to a significant incompleteness effect.

6.2 Mass-to-number density

As a second test of self-consistency between the assumptions of our analysis and the data we show in Fig. 12 the surface number density of galaxies in all clusters combined into one. The surface density was evaluated in radial bins equally spaced in logarithmic scale, where the universal scaling of radii by r_s was adopted (N_s is the number of galaxies within the $R < r_s$ aperture). The points above $3r_s$ were corrected for the incompleteness of velocity diagrams which occurs due to the fact that the value of R_{\max}/r_s is not universal in the cluster sample. As a line of reference we plotted the projected NFW profile (black solid line). Apart from radii above $\sim 3r_s$, where some deviations between the model and the data occur mostly due to the problem of incompleteness, galaxy density is well approximated by the NFW profile. Our data for small radii do not reveal a signature of a core in galaxy distribution, as advocated by Popesso et al. (2007). Although our analysis concerns the projected densities, we may conclude from Fig. 12 that the assumption of our phase-space density model about a constant mass-to-number density is also satisfied. This confirms the observational fact that has already been discussed in the literature (see e.g. Carlberg et al. 1997; Biviano & Girardi 2003).

7 SUMMARY AND CONCLUSIONS

In this paper we presented the analysis of 41 nearby ($z < 0.1$) relaxed galaxy clusters. Using the method based on the modelling of velocity diagrams in terms of the projected phase-space density, as described in section 3, we constrained parameters of the total mass and anisotropy profiles in these clusters. Parameter estimation was carried out in the framework of Bayesian data analysis with the use of the MCMC technique.

We found that the concentration parameter is weakly

correlated with the morphological type of the clusters as well as with the presence of a cool core. We interpret this fact as a signature of cluster evolution from the state with a flatter density profile (low concentration parameter) to one with a steeper density profile (higher concentration parameter). Our explanation is consistent with the recent results of cosmological simulations which predict steeper density profiles for more dynamically evolved clusters (Macciò et al. 2008; Dolag et al. 2009; Duffy et al. 2010).

The virial mass of the clusters correlates very well with the velocity dispersion, the X-ray temperature and the X-ray luminosity of the clusters. The slopes of the mass scaling relations agree with the estimates found in the literature and in the case of the velocity dispersion and X-ray temperature are consistent with the prediction from the virial theorem. We used constraints on the virial mass and the concentration parameter to test the most up-to-date estimates of the σ_8 parameter against the observational relation between the virial mass and the concentration parameter. Comparing the normalization of the mass-concentration relation for our cluster sample with the calibration from cosmological simulations we found that our data favours a rather high value, $\sigma_8 = 0.9^{+0.07}_{-0.08}$. Like Buote et al. (2007), we found an excellent agreement with σ_8 from the 1st data release of the WMAP satellite.

Our model of the projected phase-space density allowed us to constrain the profile of the orbital anisotropy in clusters. We showed at high significance level that galaxy orbits are isotropic in the cluster centres and radially anisotropic at the virial sphere, with $\beta \approx 0.65$ ($\sigma_r/\sigma_\theta \approx 1.7$). This finding is consistent with the results obtained by Biviano & Katgert (2004) for late type galaxies in nearby galaxy clusters and generalizes a number of estimates of the global anisotropy of galaxy orbits in clusters (see e.g. Lokas et al. 2006; Wojtak & Lokas 2007; van der Marel et al. 2000).

Our constraints on the asymptotic values of the anisotropy parameter implies a growth of the anisotropy from $\beta \approx 0$ at the cluster centre to $\beta \approx 0.4$ at the scale radius. Interestingly, this result agrees fairly well with recent estimates of the anisotropy for dark matter in galaxy clusters (Host et al. 2009; Hansen & Piffaretti 2007).

The orbital anisotropy at the virial sphere of the low concentration clusters tends to be more radially biased than for the clusters of high concentration parameter. We suggest that this tendency is a consequence of a change in the galaxy orbits from radially biased at the early stage of cluster evolution to more isotropic for more dynamically evolved clusters. This scenario is supported by the studies of the orbital anisotropy for different galaxy populations which reveals a similar dichotomy between early and late type galaxies representing more and less relaxed galaxy populations in the clusters (see Biviano & Katgert 2004).

ACKNOWLEDGMENTS

RW wishes to thank G. Mamon, S. Gottlöber, A. Schwöpe and G. Lamer for discussions. RW is grateful for the hospitality of Institut d'Astrophysique de Paris and Astrophysikalisches Institut Potsdam where parts of this work were done. This research has made use of the NASA/IPAC Extragalactic Database (NED) which is operated by the Jet

Propulsion Laboratory, California Institute of Technology, under contract with the National Aeronautics and Space Administration. This work was partially supported by the Polish Ministry of Science and Higher Education under grant NN203025333 as well as by the Polish-French collaboration program of LEA Astro-PF. RW acknowledges support from the START Fellowship for Young Researchers granted by the Foundation for Polish Science.

REFERENCES

- Abell G. O., 1958, *ApJS*, 3, 211
 Abell G. O., Corwin H. G., Olowin R. P., 1989, *ApJS*, 70, 1
 Adami C., Biviano A., Mazure A., 1998, *A&A*, 331, 439
 Adelman-McCarthy J. K., Agüeros M. A., Allam S. S. et al., 2008, *ApJS*, 175, 297
 An J. H., Evans N. W., 2006, *ApJ*, 642, 752
 Arnaud M., Pointecouteau E., Pratt G. W., 2005, *A&A*, 441, 893
 Bautz L. P., Morgan W. W., 1970, *ApJ*, 162, 149
 Benatov L., Rines K., Natarajan P., Kravtsov A., Nagai D., 2006, *MNRAS*, 370, 427
 Binney J., Mamon G. A., 1982, *MNRAS*, 200, 361
 Biviano A., Girardi M., 2003, *ApJ*, 585, 205
 Biviano A., Katgert P., 2004, *A&A*, 424, 779
 Borgani S., Murante G., Springel V. et al., 2004, *MNRAS*, 348, 1078
 Böhringer H., Voges W., Huchra J. P. et al., 2000, *ApJS*, 129, 435
 Böhringer H., Schuecker P., Guzzo L. et al., 2004, *A&A*, 425, 367
 Bryan G. L., Norman M. L., 1998, *ApJ*, 495, 80
 Bullock J. S., Kolatt T. S., Sigad Y., Somerville R. S., Kravtsov A. V., Klypin A. A., Primack J. R., Dekel A., 2001, *MNRAS*, 321, 559
 Buote D. A., Gastaldello F., Humphrey P. J., Zappacosta L., Bullock J. S., Brighenti F., Mathews W. G., 2007, *ApJ*, 664, 123
 Burns J. O., Hallman E. J., Gantner B., Motl P. M., Norman M. L., 2008, *ApJ*, 675, 1125
 Carlberg R. G., Yee H. K. C., Ellingson E., 1997, *ApJ*, 485, 13
 Cava A., Bettoni D., Poggianti B. M. et al., 2009, *A&A*, 495, 707
 Chen Y., Reiprich T. H., Böhringer H., Ikebe Y., Zhang Y. Y., 2007, *A&A*, 466, 805
 Colless M., Dalton G., Maddox S. et al., 2001, *MNRAS*, 328, 1039
 Comerford J. M., Meneghetti M., Bartelmann M., Schirmer M., 2006, *ApJ*, 642, 39
 Comerford J. M., Natarajan P., 2007, *MNRAS*, 379, 190
 den Hartog R., Katgert P., 1996, *MNRAS*, 279, 349
 Diaferio A., Geller M. J., 1997, *ApJ*, 481, 633
 Dolag K., Borgani S., Murante G., Springel V., 2009, *MNRAS*, 399, 497
 Duffy A. R., Schaye J., Kay S. T., Dalla Vecchia C., 2008, *MNRAS*, 390, L64
 Duffy A. R., Schaye J., Kay S. T., Vecchia C. D., Battye R. A., Booth C. M., 2010, *MNRAS*, in press

- Durret F., Lima N. G. B., Forman W., 2005, *A&A*, 432, 809
- Ettori S., De Grandi S., Molendi S., 2002, *A&A*, 391, 841
- Gastaldello F., Buote D. A., Humphrey P. J., Zappacosta L., Bullock J. S., Brighenti F., Mathews W. G., 2007, *ApJ*, 669, 158
- Gelman A., Carlin J. B., Stern H. S., Rubin D. B., 2004, *Bayesian Data Analysis*. Chapman & Hall/CRC, Boca Raton.
- Girardi M., Giuricin G., Mardirossian F., Mezzetti M., Boschini W., 1998, *ApJ*, 505, 74
- Gnedin O. Y., Kravtsov A. V., Klypin A. A., Nagai D., 2004, *ApJ*, 616, 16
- Gregory P. C., 2005, *Bayesian Logical Data Analysis for the Physical Science*
- Hansen S. H., Piffaretti R., 2007, *A&A*, 476, 37
- Heisler J., Tremaine S., Bahcall J. N., 1985, *ApJ*, 298, 8
- Horner D.J., 2001, PhD thesis, Univ. Maryland College Park
- Host O., Hansen S. H., Piffaretti R., Morandi A., Ettori S., Kay S. T., Valdarnini R., 2009, *ApJ*, 690, 358
- Hudson D. S., Mittal R., Reiprich T. H., Nulsen P. E. J., Andernach H., Sarazin C. L., 2010, *A&A*, in press
- Hwang H. S., Lee M. G., 2008, *ApJ*, 676, 218
- Isope T., Feigelson E. D., Akritas M. G., Babu G. J., 1990, *ApJ*, 364, 104
- Komatsu E., Dunkley J., Nolte M. R., Bennett C. L., Gold B., Hinshaw G., Jarosik N., Larson D., 2009, *ApJS*, 180, 330
- Ledlow M. J., Voges W., Owen F. N., Burns J. O., 2003, *AJ*, 126, 2740
- Lin Y.-T., Mohr J. J., Stanford S. A., 2004, *ApJ*, 610, 745
- Lopes P. A. A., de Carvalho R. R., Kohl-Moreira J. L., Jones C., 2009, *MNRAS*, 399, 2201
- Lokas E. L., Hoffman Y., 2001, in Spooner N. J. C., Kudryavtsev V., eds, *Proc. 3rd International Workshop, The Identification of Dark Matter*. World Scientific, Singapore, p. 121
- Lokas E. L., Mamon G. A., 2003, *MNRAS*, 343, 401
- Lokas E. L., Wojtak R., Gottlöber S., Mamon G. A., Prada F., 2006, *MNRAS*, 367, 1463
- Macciò A. V., Dutton A. A., van den Bosch F. C., 2008, *MNRAS*, 391, 1940
- Mahdavi A., Geller M. J., 2004, *ApJ*, 607, 202
- Mamon G. A., Boué G., 2010, *MNRAS*, 401, 2433
- Merrifield M. R., Kent S. M., 1990, *AJ*, 99, 1548
- Merritt D., 1987, *ApJ*, 313, 121
- Morgan W. W., Kayser S., White R. A., 1975, *ApJ*, 199, 545
- Natarajan P., Kneib J. P., 1996, *MNRAS*, 283, 1031
- Navarro J. F., Frenk C. S., White S. D. M., 1997, *ApJ*, 490, 493
- Neto A. F., Gao L., Bett P., 2007, *MNRAS*, 381, 1450
- Pedersen K., Dahle H., 2007, *ApJ*, 667, 26
- Pointecouteau E., Arnaud M., Pratt G. W., 2005, *A&A*, 435, 1
- Popesso P., Biviano A., Böhringer H., Romaniello M., Voges W., 2005, *A&A*, 433, 431
- Popesso P., Biviano A., Böhringer H., Romaniello M., 2007, *A&A*, 464, 451
- Reiprich T. H., Böhringer H., 2002, *ApJ*, 567, 716
- Rines K., Geller M. J., Kurtz M. J., Diaferio A., 2003, *AJ*, 126, 2152
- Rines K., Diaferio A., 2006, *AJ*, 132, 1275
- Sanderson A. J. R., Ponman T. J., Finoguenov A., Lloyd-Davies E. J., Markevitch M., 2003, *MNRAS*, 340, 989
- Sanderson A. J. R., Edge A. C., Smith G. P., 2009, *MNRAS*, 398, 1698
- Sarazin C. L., 1988, *X-ray emission from clusters of galaxies*. Cambridge University Press, Cambridge
- Schuecker P., Böhringer H., Reiprich T. H., Feretti L., 2001, *A&A*, 378, 408
- Smith R. J., Hudson M. J., Nelan J. E. et al., 2004, *AJ*, 128, 1558
- Snowden S. L., Mushotzky R. F., Kuntz K. D., Davis D. S., 2008, *A&A*, 478, 615
- Spergel D. N., Verde L., Peiris H. V. et al., 2003, *ApJS*, 148, 175
- Spergel D. N., Bean R., Doré O. et al., 2007, *ApJS*, 170, 377
- van der Marel R. P., Magorrian J., Carlberg R. G., Yee H. K. C., Ellingson E., 2000, *AJ*, 119, 2038
- Vikhlinin A., Kravtsov A., Forman W., Jones C., Markevitch M., Murray S. S., Van Speybroeck L., 2006, *ApJ*, 640, 691
- White D. A., 2000, *MNRAS*, 312, 663
- White D. A., Jones C., Forman W., 1997, *MNRAS*, 292, 419
- Wojtak R., Lokas E. L., 2007, *MNRAS*, 377, 843
- Wojtak R., Lokas E. L., Mamon G. A., Gottlöber S., Prada F., Moles M., 2007, *A&A*, 466, 437
- Wojtak R., Lokas E. L., Mamon G. A., Gottlöber S., Klypin A., Hoffman Y., 2008, *MNRAS*, 388, 815
- Wojtak R., Lokas E. L., Mamon G. A., Gottlöber S., 2009, *MNRAS*, 399, 812
- Xu H., Jin G., Wu X.-P., 2001, *ApJ*, 553, 78